


Cavitation bubble-induced hydrodynamic loading and interfacial deformation in an air pocket

Jihoo Moon,¹ Changhwan Jang,¹ Ehsan Mahravan² and Daegyoum Kim¹ 

¹Department of Mechanical Engineering, KAIST, Daejeon 34141, Republic of Korea

²Department of Mechanical and Production Engineering, Aarhus University, Aarhus 8000, Denmark

Corresponding author: Daegyoum Kim, daegyoum@kaist.ac.kr

(Received 7 September 2024; revised 30 April 2025; accepted 21 June 2025)

The presence of trapped air on a solid surface can alter the direction of the liquid jets induced by cavitation bubbles, which prevents or reduces erosion. In this study, we numerically investigate mutual interaction between air trapped in a pocket on a wall and a nearby bubble in water, as well as the resultant hydrodynamic loading. Both the depth and radius of the cylindrical pocket are similar to the maximum bubble radius. The pressure imposed on the inner wall of the air pocket is assessed for various values of the air pocket size and the stand-off parameter. The deformation of the air pocket and the bubble is analysed in each of three sequential stages. During the bubble expansion stage, a shock wave reflects at the water–air interface of the pocket, and the wall inside the compressed pocket is protected from the shock wave. As the bubble jet induced during bubble contraction tends to move away from the air pocket, other liquid jets formed at the water–air interface, namely central and lateral pocket jets, can directly collide with the inner wall of the pocket after the bubble collapses. These collisions exert significant pressure on the wall under certain conditions. The formation of the central pocket jet originates from the strong fluctuation of the water–air interface by the expanding and contracting bubble. The development of the lateral pocket is related to changes in the potential energy of the air under its second contraction.

Key words: cavitation, interfacial flows (free surface)

1. Introduction

The interaction between a collapsing bubble immersed in a liquid and a neighbouring boundary has been investigated for several decades. A notable phenomenon observed

during the collapse of a bubble is the creation of a liquid jet, also known as a bubble jet, by the asymmetric pressure distribution near the collapsing bubble. The bubble jet induced by the collapsing bubble typically has a high speed and a narrow tip, making it useful in applications such as needle-free injection (Kyriazis, Koukouvinis & Gavaises 2019; Gálvez *et al.* 2020; Robles *et al.* 2020), laser-induced forward transfer (Turkoz *et al.* 2018; Kalaitzis *et al.* 2019; Theodorakos *et al.* 2019; Mahravan & Kim 2021), and surface cleaning (Verhaagen & Rivas 2016; Wang *et al.* 2020; Jin *et al.* 2022). However, one negative aspect of bubble jets is the significant hydrodynamic loading that they can induce, and the resultant damage to walls near the location of cavitation inception.

The uneven pressure distribution near a cavitation bubble depends on adjacent boundaries. Hence the effects of different adjacent boundaries on the behaviour of a bubble have been widely studied. A bubble in proximity to a rigid wall induces a bubble jet that moves towards the wall during the contraction and collapse of the bubble (Lauterborn & Bolle 1975; Brujan *et al.* 2002; Tomita *et al.* 2002; Zhang *et al.* 2022). When exposed to a shear flow, a bubble near a rigid wall becomes distorted and generates two jets in different directions (Bhola *et al.* 2025). When a distant wall is placed in parallel to the rigid wall, the jet velocity increases as the distance between the two walls decreases (Zeng *et al.* 2024). Moreover, near a wall with a ridge pattern, a bubble either collapses towards the wall or is split by a radial jet (Kim & Kim 2020). In the presence of a corner geometry, the bubble jet is directed to the corner and tends to incline towards the closer wall (Brujan *et al.* 2018; Wang *et al.* 2020). If the adjacent wall is elastic, then both the stand-off parameter and the elasticity of the solid affect the dynamics of a cavitation bubble (Brujan *et al.* 2001*a,b*). A noticeable phenomenon of a cavitation bubble near an elastic solid is the formation of two axial jets in opposite directions for a specific range of the stand-off parameter, which occurs once an annular jet has been induced by the elasticity of the solid. Regarding viscoelastic solids, the ratio of two time scales characterising the viscoelastic solid deformation and bubble dynamics is a key parameter in determining the fluid–solid interactions over the entire lifespan of the bubble; the behaviour is distinctly different from that of an elastic solid (Moon, Mahravan & Kim 2024). Similarly, Abbondanza, Gallo & Casciola (2024) studied the interaction of microbubbles with an elastoplastic boundary, and showed that the asymmetric collapse of the bubble drives the plastic deformation of the surface. For a bubble near the free surface, the bubble jet was found to point away from the free surface (Blake & Gibson 1981; Robinson *et al.* 2001; Li *et al.* 2019). Furthermore, many studies have investigated bubble dynamics and jetting under particular boundary conditions, including an oil droplet attached to a rigid boundary (Ren *et al.* 2023), a granular boundary (Sieber, Preso & Farhat 2022), a fluid–fluid interface (Han *et al.* 2022) and a porous plate (Andrews, Rivas & Peters 2023).

Recently, as a means of mitigating cavitation erosion, several studies have focused on cavitation bubbles near solid surfaces in which air is entrapped within a micro-scale cavity. Gonzalez-Avila *et al.* (2020) investigated the coalescence of entrapped air with a cavitation bubble by varying the stand-off parameter and the distance between cavities. They adopted a special shape for the cavity (termed the re-entrant cavity), which has a volume similar to the maximum bubble volume and a narrow mushroom-shaped entrance to entrap the air. Sun *et al.* (2022*a*) compared the dynamics of a cavitation bubble near a solid surface using various surface geometries, such as a flat wall and an array of cavities filled with water or air. The bubble jet was found to be directed towards the wall in the case of a flat wall or a cavity filled with water, but reverses its direction when the cavity is filled with air. Furthermore, when a single cavity exists without other cavities, the bubble jet is directed away from the cavity, similar to previous studies, such as Sun *et al.* (2022*b*). In their study,

the narrow cylindrical entrance of the cavity was similar in size to the maximum bubble radius, whereas the cavity had a much larger volume than the maximum bubble volume.

The bubble behaviour is affected by other geometric conditions, even when an air cavity is present. According to Yin *et al.* (2023), because the jet direction is determined by the combined effect of the cavity entrance area and the nearby wall area, the direction of the bubble jet is effectively controlled by the size of the cylindrical cavity entrance. Sun *et al.* (2023) observed that the deflection of the bubble depends on the relative vertical and radial locations of the bubble with respect to a cavity with a cylindrical entrance. The bubble deflection was explained by the attractive effect of the solid wall and the repulsive effect of the gas-containing cavity. Although the dynamics of cavitation bubbles near a single or multiple cavities with entrapped gas has been revealed by previous studies, the magnitude of hydrodynamic loading exerted on the cavity by the bubble remains unclear. This parameter is essential in evaluating the effectiveness of gas-trapped cavities for alleviating the erosion and damage caused by the bubble.

In this study, we numerically investigate the interaction of a cavitation bubble in water with an air pocket (a cylindrical cavity without a re-entrant or other special entrance shape) on a rigid wall. Specifically, we focus on the water–air interface in the air pocket, and the consequent hydrodynamic loading exerted on the wall. The radius and depth of the cylindrical air pocket and the distance between the point of bubble inception and the air pocket are varied. The numerical model and methods are described in § 2. In § 3.1, the characteristics of hydrodynamic loading are first identified through comparisons with those of a rigid flat wall without an air pocket. The entire interaction process is divided into three stages: bubble expansion and air pocket contraction (§ 3.2), bubble contraction and air pocket expansion (§ 3.3), and pocket jet formation (§ 3.4). In § 3.2, the reflection of a shock wave propagating from the expanding bubble by the air pocket and the collision of water with a wall are examined. The formation and speed of the bubble jet are analysed, along with its coupling with expanding air in the pocket, in § 3.3. Furthermore, the dynamics of the pocket jet that emerges from the water–air interface in the air pocket and the associated hydrodynamic loading are discussed in § 3.4. Finally, our findings are summarised in § 4.

2. Problem description

2.1. Model and parameters

We consider a single cylindrical air pocket within an upper rigid wall and a high-pressure micro-scale bubble immersed in water (figure 1a). For simplicity, the centres of the bubble and the air pocket in the initial state are positioned on the axis of symmetry, and the flow is assumed to be axisymmetric; this can be justified by the axisymmetric physical configuration in the initial state, and the very short duration of the entire process. The radius R_p and depth H_p of the air pocket are varied to assess the effects of the air pocket geometry. The dimensionless parameters $R^* = R_p/R_{unb,max}$ and $H^* = H_p/R_{unb,max}$, as well as the stand-off parameter $\gamma = L/R_{unb,max}$, are used as variables: $R^* = [1.0, 2.1]$, $H^* = 0.2–1.3$ and $\gamma = 0.5–2.5$. Here, $R_{unb,max}$ is the maximum radius of an unbounded bubble (with no nearby solid) during expansion, and L is the distance between the initial bubble centre and the initial water–air interface of the air pocket. To avoid a weak interaction between the air pocket and the bubble, the upper limit of γ is set to 2.5. A very small distance between the air pocket and the bubble may cause violent distortions of the water–air interface. Thus the minimum value of γ is limited to 0.5. For the case of a flat wall without an air pocket, the area of the wall affected by a nearby cavitation bubble

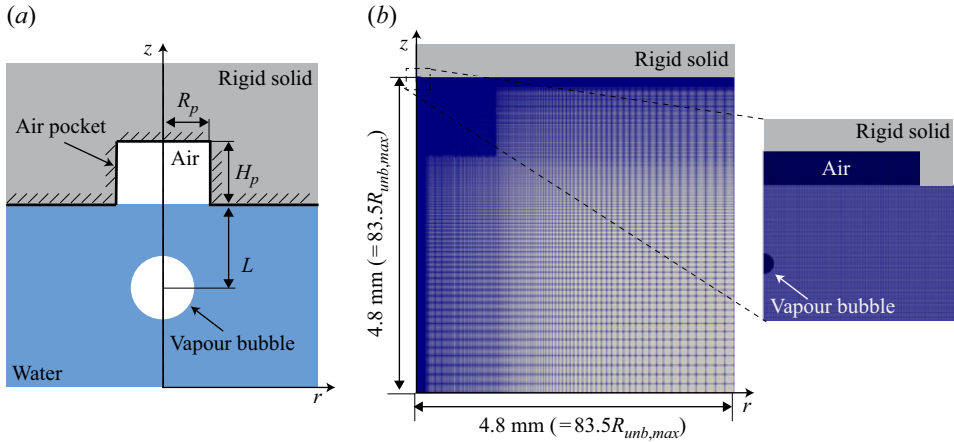


Figure 1. (a) Schematic of a bubble immersed in water and an air pocket on an upper rigid wall. (b) Axisymmetric two-dimensional fluid domain for numerical simulations. The z -axis is treated as the axisymmetric axis.

depends on the stand-off parameter (Philipp & Lauterborn 1998). The range of R^* in this study is chosen to cover most of the area primarily affected by a nearby cavitation bubble for the considered range of the stand-off parameter. For all cases, the initial radius and inner pressure of the bubble are $R_0 = 4 \text{ } \mu\text{m}$ and $p_{g,0} = 147 \times 10^6 \text{ Pa}$, respectively. Here, $R_{unb,max}$ is calculated from the initial bubble pressure and radius, which is explained later. Under this initial condition, the maximum expansion radius of the bubble varies slightly depending on the surrounding environment, but generally ranges from approximately $50 \text{ } \mu\text{m}$ to $60 \text{ } \mu\text{m}$. This particular length scale is chosen because it is relevant to a wide range of biomedical and industrial applications, and it aligns with the range observed in many previous studies that investigated the interactions between bubbles and various types of boundaries ranging from a few to hundreds of micrometres (e.g. Philipp & Lauterborn 1998; Brujan *et al.* 2001a; Gonzalez-Avila *et al.* 2020; Zeng *et al.* 2024; Bhola *et al.* 2025).

Because the expansion and contraction of a bubble occur very rapidly, heat transfer between the phases is negligible (Vogel & Lauterborn 1988; Miller *et al.* 2013; Koukouvinis *et al.* 2016; Zeng *et al.* 2018). This assumption allows us to exclude temperature from the equation of state, eliminating the need to solve the energy conservation equation. The Tait equation (2.1a) is chosen as the equation of state for water, and the adiabatic process (2.1b) is assumed for the air in the pocket and the gas in the bubble:

$$\rho = \rho_{ref} \left(\frac{p + B}{p_{\infty} + B} \right)^{1/n}, \quad \rho = \rho_{ref} \left(\frac{p}{p_{ref}} \right)^{1/\kappa}. \quad (2.1a,b)$$

The parameters in the Tait equation (2.1a) are the reference density $\rho_{ref} = 1.0 \times 10^3 \text{ kg m}^{-3}$, atmospheric pressure $p_{\infty} = 1.0 \times 10^5 \text{ Pa}$, $B = 3.0 \times 10^5 \text{ Pa}$, and $n = 7.2$. The parameters for the air in the pocket and the vapour gas in the bubble in (2.1b) are $\rho_{ref,air} = 1.2 \text{ kg m}^{-3}$, $p_{ref,air} = 1.0 \times 10^5 \text{ Pa}$, $\rho_{ref,bub} = 0.6 \text{ kg m}^{-3}$, $p_{ref,bub} = 1.4 \times 10^5 \text{ Pa}$, and $\kappa = 1.4$. The reference density of the air or the gas is set to its density at $100 \text{ } ^\circ\text{C}$. The reference pressure is calculated as $p_{\infty} + 2\sigma/R_0$, where the second term is neglected for the air in the pocket. The surface tension coefficients for

the water–air interface (of the air pocket) and the water–gas interface (of the bubble) are 7.28×10^{-2} and $7.25 \times 10^{-2} \text{ N m}^{-1}$, respectively.

Under the above-mentioned initial conditions of the bubble, $R_{unb,max}$ is calculated using the Rayleigh–Plesset model and the Gilmore model (Gilmore 1952). The Rayleigh–Plesset equation and Gilmore equation are numerically solved by the fourth- and fifth-order Runge–Kutta methods, respectively. The maximum bubble radius calculated by the Rayleigh–Plesset model is $60.0 \text{ }\mu\text{m}$, while the Gilmore model yields the value $57.5 \text{ }\mu\text{m}$. The Gilmore model accounts for the compressibility of the liquid, unlike the Rayleigh–Plesset model. Thus we use $R_{unb,max} = 57.5 \text{ }\mu\text{m}$ as the reference bubble size. The Gilmore equation is expressed as

$$R \frac{d^2 R}{dt^2} \left(1 - \frac{1}{c} \frac{dR}{dt} \right) + \frac{3}{2} \left(\frac{dR}{dt} \right)^2 \left(1 - \frac{1}{3c} \frac{dR}{dt} \right) = H \left(1 + \frac{1}{c} \frac{dR}{dt} \right) + \frac{R}{c} \frac{dH}{dt} \left(1 - \frac{1}{c} \frac{dR}{dt} \right), \quad (2.2)$$

where

$$H = n \left(\frac{p_\infty + B}{(n-1)\rho_{l,int}} \right) \left[\left(\frac{p+B}{p_\infty + B} \right)^{(n-1)/n} - 1 \right], \quad (2.3a)$$

$$c = c_\infty \left(\frac{p+B}{p_\infty + B} \right)^{(n-1)/2n}, \quad (2.3b)$$

$$c_\infty = \left[n \left(\frac{p_\infty + B}{\rho_{l,int}} \right) \right]^{1/2}, \quad (2.3c)$$

$$p_{l,int} = p_{g,0} \left(\frac{R_0}{R} \right)^{3\kappa} + p_v - \frac{2\sigma}{R} - 4\mu_l \frac{1}{R} \frac{dR}{dt}, \quad (2.3d)$$

with $\rho_{l,int} = 1.0 \times 10^3 \text{ kg m}^{-3}$, $c_\infty = 1.5 \times 10^3 \text{ m s}^{-1}$, $p_v = 2.3 \times 10^3 \text{ Pa}$, $\sigma = 7.25 \times 10^{-2} \text{ N m}^{-1}$, $\mu_l = 1.0 \times 10^{-3} \text{ Pa s}$ and $p_{l,int}$ denoting the density of the liquid (water in this study) at the bubble interface, speed of sound at infinity, vapour pressure of the bubble, surface tension coefficient of the bubble interface, dynamic viscosity of the liquid, and pressure of the liquid at the bubble interface, respectively.

2.2. Numerical methods

Numerical simulations are conducted using a revised code from OpenFOAM (Weller *et al.* 1998). The compressible PISO algorithm (Issa 1986) is employed to solve the mass and momentum conservation equations:

$$\frac{\partial \rho}{\partial t} + \nabla \cdot (\rho \mathbf{u}) = 0, \quad (2.4a)$$

$$\frac{\partial (\rho \mathbf{u})}{\partial t} + \nabla \cdot (\rho \mathbf{u} \mathbf{u}) = -\nabla p + \rho \mathbf{g} + \nabla \cdot \boldsymbol{\tau} + \mathbf{f}_{surf}, \quad (2.4b)$$

where ρ is fluid density, \mathbf{u} is velocity, p is pressure, \mathbf{g} is gravitational acceleration, $\boldsymbol{\tau}$ is viscous stress, and \mathbf{f}_{surf} is surface tension force per unit volume. The surface tension force term \mathbf{f}_{surf} in each cell, modelled as a continuum surface force in each cell, is computed as (Brackbill, Kothe & Zemach 1992)

$$\mathbf{f}_{surf} = \sum_{i,j=1, i < j}^3 \sigma_{i,j} K_{i,j} (\alpha_j \nabla \alpha_i - \alpha_i \nabla \alpha_j), \quad (2.5)$$

where the subscripts i and j denote each immiscible fluid (water, air or gas), σ is the surface tension coefficient, K is the curvature of the interface, and α is the volume fraction of a fluid in a cell. Here, $K_{i,j}$ is determined by

$$K_{i,j} = -\nabla \cdot \frac{\alpha_j \nabla \alpha_i - \alpha_i \nabla \alpha_j}{\|\alpha_j \nabla \alpha_i - \alpha_i \nabla \alpha_j\|}. \quad (2.6)$$

The volume of fluid method is used to capture the interface between the three different phases. It is assumed that no evaporation or condensation occurs during the entire process because the duration of the bubble collapse is extremely short (Kobayashi *et al.* 2018). For any cell, the volume fractions α_i of the three fluids should satisfy $\alpha_1 + \alpha_2 + \alpha_3 = 1$. This condition is ensured by the semi-implicit and second-order version of the multidimensional universal limiter for explicit solution (MULES) algorithm in OpenFOAM (Weller 2008). For each phase, the following equation, which is a generalised form of the two-phase volume of fluid method (Koch *et al.* 2016), is solved to obtain the volume fraction:

$$\begin{aligned} \frac{\partial \alpha_i}{\partial t} + \nabla \cdot (\alpha_i \mathbf{u}) + \nabla \cdot \left[\alpha_i \left(1 - \sum_{k=1, k \neq i}^3 \alpha_k \right) \mathbf{u}_r \right] \\ = \sum_{k=1, k \neq i}^3 \alpha_i \alpha_k \left(\frac{\psi_k}{\rho_k} - \frac{\psi_i}{\rho_i} \right) \frac{Dp}{Dt} + \alpha_i \nabla \cdot \mathbf{u}, \end{aligned} \quad (2.7)$$

where ψ is defined as $D\rho/Dp$, and D/Dt is the material derivative. At the face of each cell, \mathbf{u}_r is defined as $c_\alpha |\phi_f| |\mathbf{n}_f| / |\mathbf{A}_f|$, where c_α , ϕ_f , \mathbf{n}_f and \mathbf{A}_f are the interface compression parameter (0.5), volume flux through the face, unit vector normal to the interface between the two fluids, and normal vector whose magnitude is the area of the face, respectively. Note that the dynamic contact angle is not considered in this study although it may be crucial in determining the deformation of the water–air interface for micro-scale geometry, and the static contact angle of the water–air interface on the wall is set to 90° . The effect of different contact line dynamics is not within the scope of the current study.

To reduce the computational cost, a two-dimensional axisymmetric domain is adopted (figure 1b). The width and height of the domain are set to $83.5 R_{unb,max}$ ($= 4.8$ mm), which is sufficiently large such that the reflection of a pressure pulse on the domain boundary can be minimised. A no-slip boundary condition for the velocity is applied on the wall. To minimise the boundary effect, a zero-gradient velocity in the normal direction and a non-reflective condition for the pressure are adopted for the outer boundaries, except for the wall.

In each time step, the mass and momentum conservation equations (2.4) are considered after solving the volume fraction equation (2.7). The fluid properties required to solve (2.4) are obtained from $\rho = \sum_{i=1}^3 \alpha_i \rho_i$ and $\mu = \sum_{i=1}^3 \alpha_i \mu_i$. The Euler implicit scheme is employed for temporal discretisation. Gradient terms, Laplacian terms and the divergence terms of the viscous stress tensor are discretised using the second-order linear scheme. In addition, the interpolation of cell-centred quantities to cell faces is also performed using the same linear scheme to ensure consistency. Convection terms are discretised using the second-order MUSCL scheme. To sufficiently resolve rapid fluid motions such

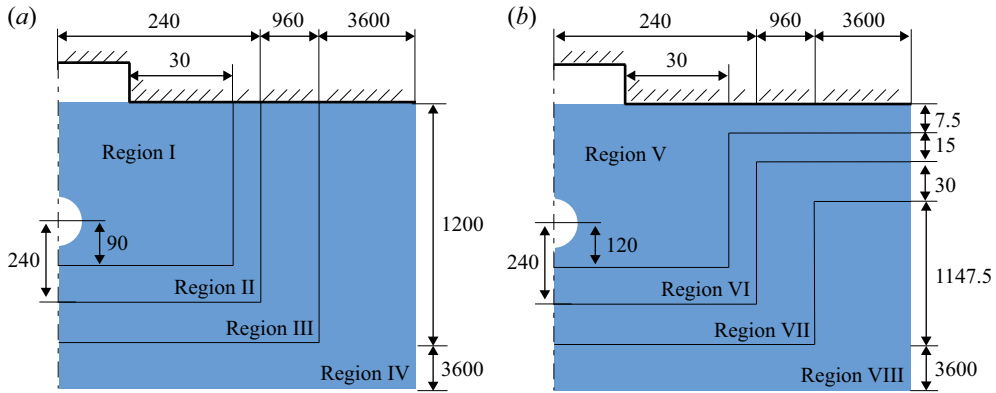


Figure 2. Regions for (a) initial grid formation and (b) iterative grid refinement of the initial configuration. The units are μm .

as shock wave propagation, bubble collapse and jet propagation, the initial time step is set to 1.2×10^{-11} s, and the time step is adjusted dynamically such that the maximum Courant–Friedrichs–Lewy (CFL) number remains under 0.1. The CFL number of each cell is defined as $\sum_f |\mathbf{u}_f \cdot \mathbf{A}_f| \Delta t / (2V_{cell})$; here, the subscript f represents cell faces, and Δt and V_{cell} are the previous time step size and the volume of the cell, respectively. The summation is iterated over all faces of the cell. With this condition, the acoustic CFL number $\sum_f (|\mathbf{u}_f \cdot \mathbf{A}_f| + c_l A_f) \Delta t / (2V_{cell})$ based on the speed of sound in water ($c_l \approx 1477 \text{ m s}^{-1}$) remains below 1.0 during key phases where compressibility plays a critical role – namely, during shock propagation, rapid initial expansion of the bubble, and its collapse followed by secondary expansion.

2.3. Grid convergence test and validation

The grid layout for the numerical simulations is generated through iterative refinement of an initial configuration consisting of both uniform and non-uniform cells. The fluid domain can be divided into four regions by the growth rate of cell size in the radial and axial directions (figure 2a). Region I consists of uniform cells with size $0.2 \mu\text{m}$. Regions II and III have a constant growth rate of cell size, so the average numbers of cells per unit length along the radial and axial directions are a half and a quarter of those in region I, respectively. Region IV has 15 cells in both the radial and axial directions. After establishing the initial grid layout, several refinements are applied to better resolve the water–air and water–gas interfaces (figure 2b). In figure 2(b), regions V–VII are refined four times, twice and once, respectively, while region VIII remains unrefined from the initial set-up.

To confirm that the refined grid is appropriate, two grid convergence tests are performed: a case with an air pocket with $R^* = 1.0$, $H^* = 0.9$ and $\gamma = 1.7$, and a case without an air pocket with $\gamma = 1.7$ (figure 3). In figures 3(a) and 3(b), $V_{air,min}$, $V_{air,max}$ and $V_{air,0}$ represent the minimum, maximum and initial volumes of air inside the pocket, respectively. The parameter N denotes the number of cells constituting the initial bubble radius. The volume of the air is calculated by summing the product of the air volume fraction and the cell volume across the entire domain. Variations in $V_{air,min}/V_{air,0}$ with respect to N are negligible. By contrast, $V_{air,max}/V_{air,0}$ decreases appreciably as N increases from 10 to 20. For both quantities, the error relative to the $N = 60$ case does not decrease monotonically with grid refinement, which may be influenced by nonlinear

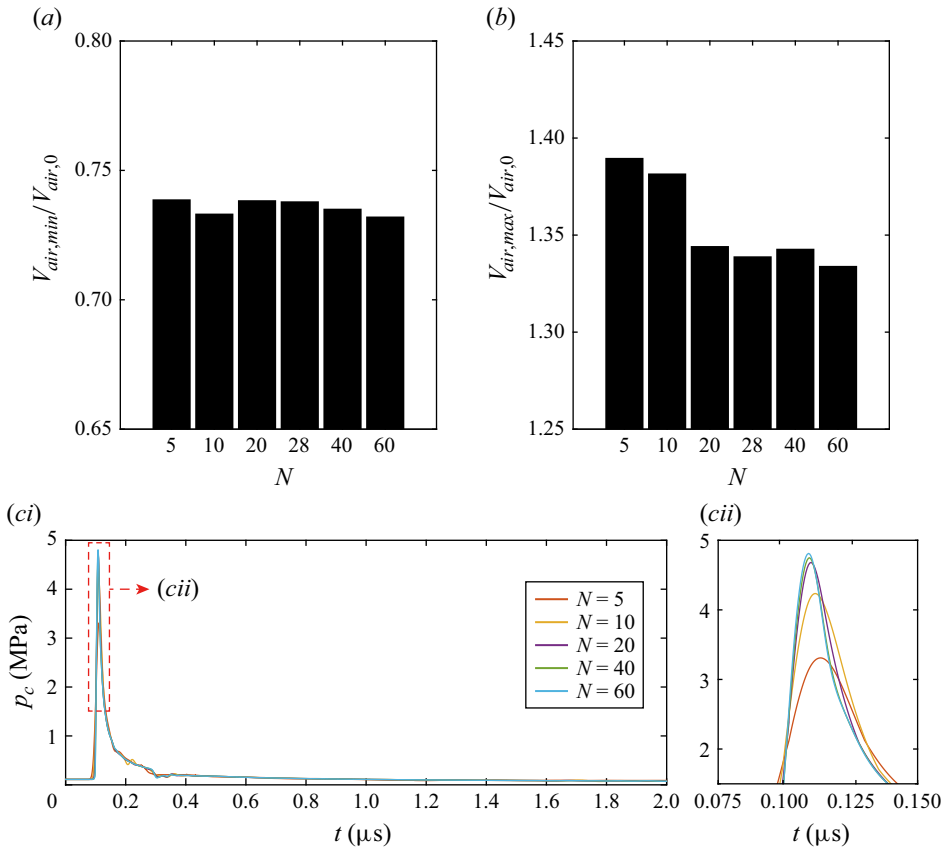


Figure 3. Grid convergence test for $R^* = 1.0$, $H^* = 0.9$ and $\gamma = 1.7$: (a) normalised minimum volume of air in the pocket, $V_{air,min}/V_{air,0}$, and (b) normalised maximum volume of air in the pocket, $V_{air,max}/V_{air,0}$. (c) Grid convergence test for the case without an air pocket ($\gamma = 1.7$): time history of pressure on wall centre, p_c .

interactions between the bubble and air pocket. Nevertheless, the differences with respect to the $N = 60$ case are less than 1.0 % for $N \geq 20$, suggesting that the cell size of the $N = 20$ case (used for our numerical simulations) is a reasonable choice. The case without an air pocket is specifically considered to check the grid convergence of the pressure acting on the wall centre, p_c ; this case is chosen because the shock generated by the initial bubble expansion imposes a strong pressure peak on the wall centre. In figure 3(c), as N increases to 60, the time history of p_c converges to a certain curve. Moreover, for $N \geq 20$, the peak pressure values exhibit a discrepancy of less than 1.0 % compared to the $N = 60$ case, and the instants of the peak are almost identical.

The numerical method of this study is validated by comparing the results for a cavitation bubble near a free surface with the numerical and experimental results from a previous study (Li *et al.* 2019). As the dynamics of the water–air interface inside the air pocket are of particular interest, the bubble near the free surface is chosen as a physical model for validation. We adopt the numerical conditions (e.g. maximum CFL number, boundary conditions) and physical conditions (e.g. initial bubble condition, equation of state) used in Li *et al.* (2019). To match their configuration, gas replaces air above the water–air interface, and the wall (and the pocket) is removed. The temporal evolution of two interfaces in the present study is very similar to that of Li *et al.* (2019) (figure 4a). Noticeable events, such

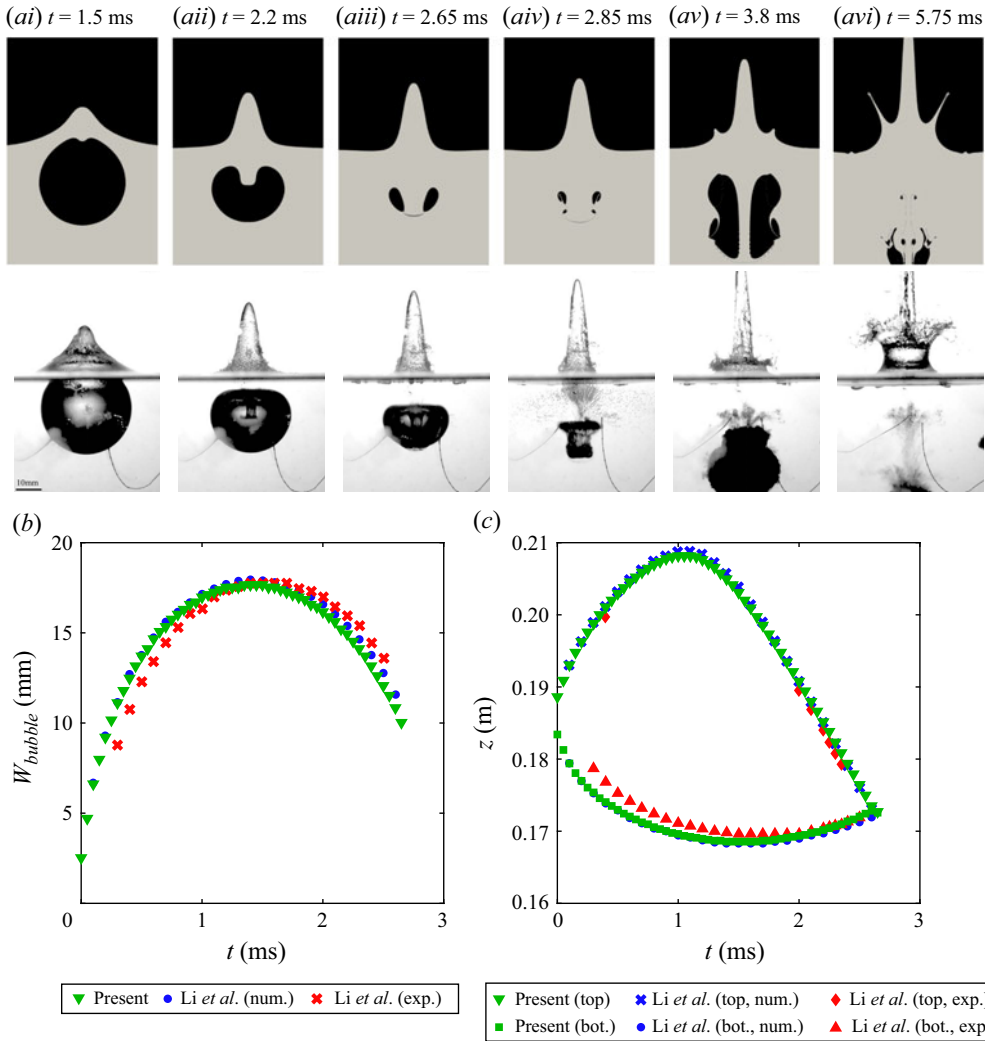


Figure 4. Comparison of results for a cavitation bubble near a free surface with Li *et al.* (2019). (a) Temporal evolution of the free surface and the bubble from the numerical result of the present study (upper) and the experimental result of the reference (lower). (b) Width of the bubble and (c) locations of its top-most and bottom-most points. The green, blue and red markers represent the numerical result of the present study and the numerical and experimental results of Li *et al.* (2019), respectively. Reproduced from Li *et al.* (2019), with the permission of AIP Publishing.

as the bubble jet penetration (bubble collapse) and the formation of the central spike and water skirt, occur at similar times in both simulations. Half of the maximum bubble width W_{bubble} , and the locations of its top-most and bottom-most points along the z -axis before contact between the upper and lower surfaces of the contracting bubble, are presented in figures 4(b) and 4(c). The differences among the results are minor, so we can conclude that the numerical method of this study is reliable for predicting the motion of a water–air interface and the expansion/collapse of a bubble. For further validation of our numerical method, readers are referred to our previous work (Moon *et al.* 2024), which provides additional evidence of its ability to accurately capture shock wave propagation and bubble dynamics near a rigid or elastic boundary.

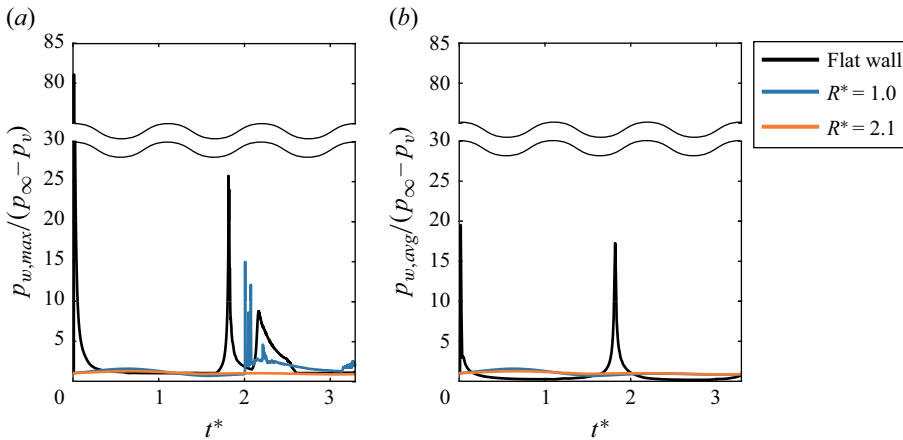


Figure 5. Time histories of (a) maximum pressure $p_{w,max}$ and (b) average pressure $p_{w,avg}$ on the flat wall ($\gamma = 1.7$) and the wall with an air pocket ($R^* = [1.0, 2.1]$, $H^* = 0.9$, $\gamma = 1.7$).

3. Results and discussion

3.1. Hydrodynamic loading on a wall

First, we evaluate the effects of an air pocket on the hydrodynamic loading exerted on a wall (figure 5). Here, we focus on a horizontal wall (ceiling) inside the air pocket to assess the hydrodynamic loading; the effective stand-off distance from the bubble centre to the horizontal wall of interest is $\gamma + H^*$. The pressure p_w on the horizontal wall inside the air pocket, and time t , are made dimensionless by $p_{\infty} - p_v$ and t_{ref} , respectively, where the reference time scale t_{ref} is defined as $R_{unb,max}[\rho/(p_{\infty} - p_v)]^{1/2}$ (Lauterborn & Bolle 1975; Brujan *et al.* 2002); the dimensionless time is given by $t^* = t/t_{ref}$. In figure 5, the subscripts *max* and *avg* for p_w indicate the maximum pressure at any location on the horizontal wall, and the spatially averaged pressure on the horizontal wall for a given instant, respectively. The average pressure $p_{w,avg}$ is calculated on a circular area of the wall that has a radius equivalent to $R_{unb,max}$.

For all flat wall cases with no air pocket, two sharp peaks appear for each of $p_{w,max}$ and $p_{w,avg}$ through a lifespan of the bubble (figure 5a,b). The first peak appears when a shock wave from the bubble reaches the wall at the beginning of bubble expansion, while the second peak occurs when the bubble jet impinges on the wall after the collapse of the bubble. In most air pocket cases, however, both peaks of $p_{w,max}$ are suppressed, as illustrated by the coloured lines in figure 5(a). In particular, the first peak (caused by the shock wave) vanishes completely in all cases. In several air pocket cases, the second peak of $p_{w,max}$ is significantly higher than that in the flat wall cases. The second peak is induced by a liquid jet at the water–air interface, which is analysed in detail in § 3.4. Because the pressure is spatially averaged for calculating $p_{w,avg}$, the two peaks of $p_{w,avg}$ disappear in the presence of an air pocket, in contrast to $p_{w,max}$ (figure 5b).

The rationale behind the change in the hydrodynamic loading is attributed to the interaction between the bubble and the entrapped air in the pocket. The detailed mechanism of the interaction between the bubble and the air pocket, and its effects on hydrodynamic loading, are analysed in each of the three sequential stages in §§ 3.2–3.4. Because surface erosion and damage are more closely related to the maximum pressure than the average pressure, our emphasis hereafter is primarily on the maximum pressure $p_{w,max}$.

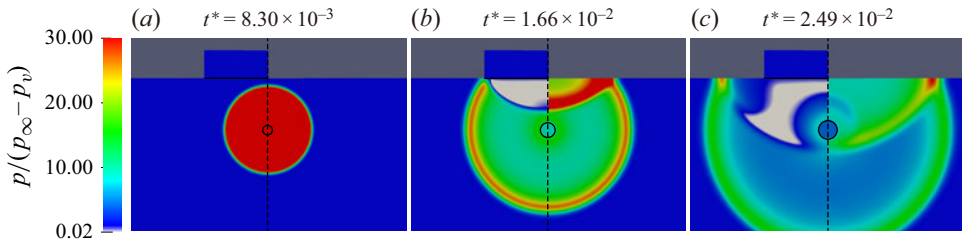


Figure 6. Temporal evolution of pressure during bubble expansion for the air pocket case (left, $R^* = 2.1$, $H^* = 0.9$, $\gamma = 1.7$) and the flat wall case (right, $\gamma = 1.7$). The grey area indicates the vapour pressure region, and the black solid lines indicate the interfaces between the two phases. See supplementary movie 1.

3.2. Bubble expansion and air pocket contraction

The high internal pressure of the initial bubble generates a shock wave that propagates outwards from the bubble (see figure 6 and supplementary movie 1). In the flat wall cases, once the shock wave reaches the wall, high pressure is exerted on the wall, leaving a noticeable pressure peak in figure 5(a). A reflected wave then propagates back towards the bubble from the wall, maintaining a high-pressure zone near the wall. By contrast, in the air pocket cases, the shock is not transmitted through the interface, so the horizontal wall (ceiling) inside the air pocket does not experience high pressure caused by the shock wave. This different result can be attributed to acoustic impedance (Wang *et al.* 2014), which is defined as the product of density and the speed of sound. Because the acoustic impedance of water greatly exceeds that of air, the shock wave transmitted through the water–air interface is much weaker than a reflected wave. The incident wave and the reflected wave combine to generate a rarefaction wave by destructive interference, and the pressure drops significantly in the region between the bubble and the water–air interface. In this region, the pressure reaches vapour pressure ($p_v = 2.3 \times 10^3$ Pa) as indicated by the grey area at $t^* = 1.66 \times 10^{-2}$ and 2.49×10^{-2} in figure 6, which is the lower bound of the simulation. Actually, such low pressure may lead to the vaporisation of water and the creation of small cavitation bubbles (Horvat *et al.* 2022). However, because the duration of this low-pressure zone is extremely short, the associated phase change phenomena are not considered in the simulation. The grey region disappears within a few hundred nanoseconds after the passage of the shock, as can be observed in supplementary movie 1.

Within a very short time from the initial state, the bubble undergoes rapid expansion, with its volume increasing by a factor of several hundred compared with the initial volume, because of the high internal pressure at the start (figure 7). The expansion reduces the volume of air trapped within the pocket. As the bubble continues to expand, the rate of volume increase slows due to a decrease in the internal pressure. Similarly, the contraction rate of the air within the pocket decreases. In the meantime, a hump develops at the edge of the pocket, as demonstrated in the inset of figure 7(c). The motion of the hump and its evolution into a liquid jet are analysed in § 3.4.

The temporal peak value of $p_{w,max}$ during the stage of bubble expansion, $p_{w,max,exp}$, is shown in figure 8 for different values of the pocket radius R^* , pocket height H^* , and stand-off parameter γ . In both the flat wall and air pocket cases, $p_{w,max,exp}$ decreases as γ increases. The trend in $p_{w,max,exp}$ is analysed by considering the cause of the pressure on the wall. For the flat wall cases, the effect of the shock wave from the expanding bubble obviously diminishes as the bubble position moves farther away from the wall. The trend in $p_{w,max,exp}$ with respect to γ persists in the cases with an air pocket, but $p_{w,max,exp}$ exhibits a very abrupt change around $\gamma = 1.0$, unlike in the flat wall case. In most air

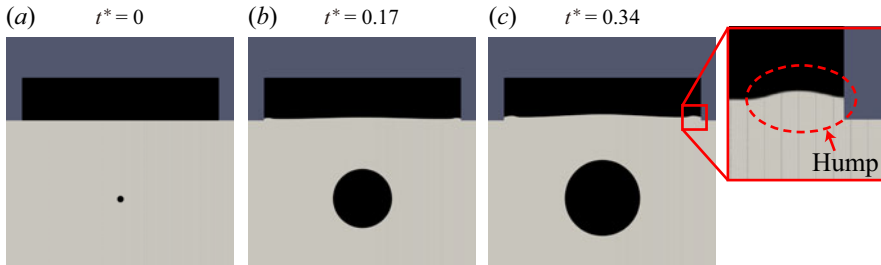


Figure 7. Temporal evolution of bubble expansion and air pocket contraction ($R^* = 2.1$, $H^* = 0.9$, $\gamma = 1.7$). The black and light grey regions indicate gaseous (air/bubble gas) and liquid phases, respectively.

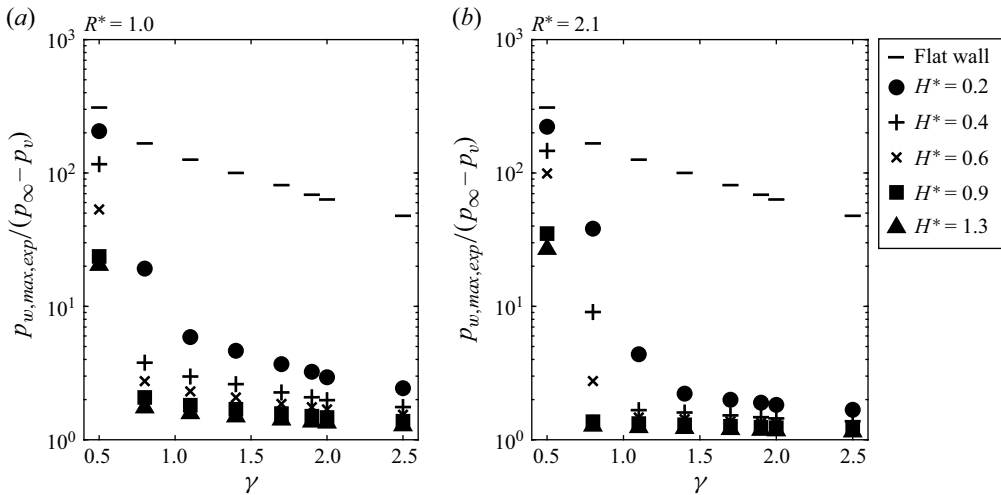


Figure 8. Peak pressure $p_{w,max,exp}$ on the wall during bubble expansion for the flat wall and air pocket cases: (a) $R^* = 1.0$ and (b) $R^* = 2.1$. The pressure in (a) and (b) is drawn on a logarithmic scale.

pocket cases where γ is greater than approximately 1.0, the peak pressure is only several times greater than the atmospheric pressure, i.e. $p_{w,max,exp}/(p_\infty - p_v) < 10$. However, even when the air pocket is present, the peak pressure can be significantly high for small $\gamma < 1.0$, i.e. $p_{w,max,exp}/(p_\infty - p_v)$ up to 200. Because there is only a small distance between the bubble and the water–air interface when γ is small, the water–air interface is strongly pushed by the expanding bubble and may collide with the ceiling inside the air pocket (see figure 9(a) and supplementary movie 2), resulting in high pressure on the wall as shown in figure 8. In figure 9(b,c), the cases with water collision are marked as purple circles. In addition to γ , the pocket depth H^* influences the occurrence of water collision with the wall. The water tends to contact the wall when H^* is sufficiently small for $\gamma = 0.8$ and 1.1, and with any value of H^* for $\gamma = 0.5$.

The maximum pressure on the wall caused by water collision, $p_{collision}$, is correlated with the collision speed of the water, $U_{collision}$ (figure 9d). Here, $U_{collision}$ is defined as the vertical speed of the water–air interface along the vertical axis of the pocket ($r = 0$) at the time step immediately before the collision. The collision speed is normalised by the reference speed U_{ref} , which is calculated as $U_{ref} = R_{unb,max}/t_{ref} = [(p_\infty - p_v)/\rho]^{1/2}$. The upper limit for the pressure caused by water collision can be predicted theoretically in terms of the water collision speed, which is presented as the dashed line in figure 9(d).

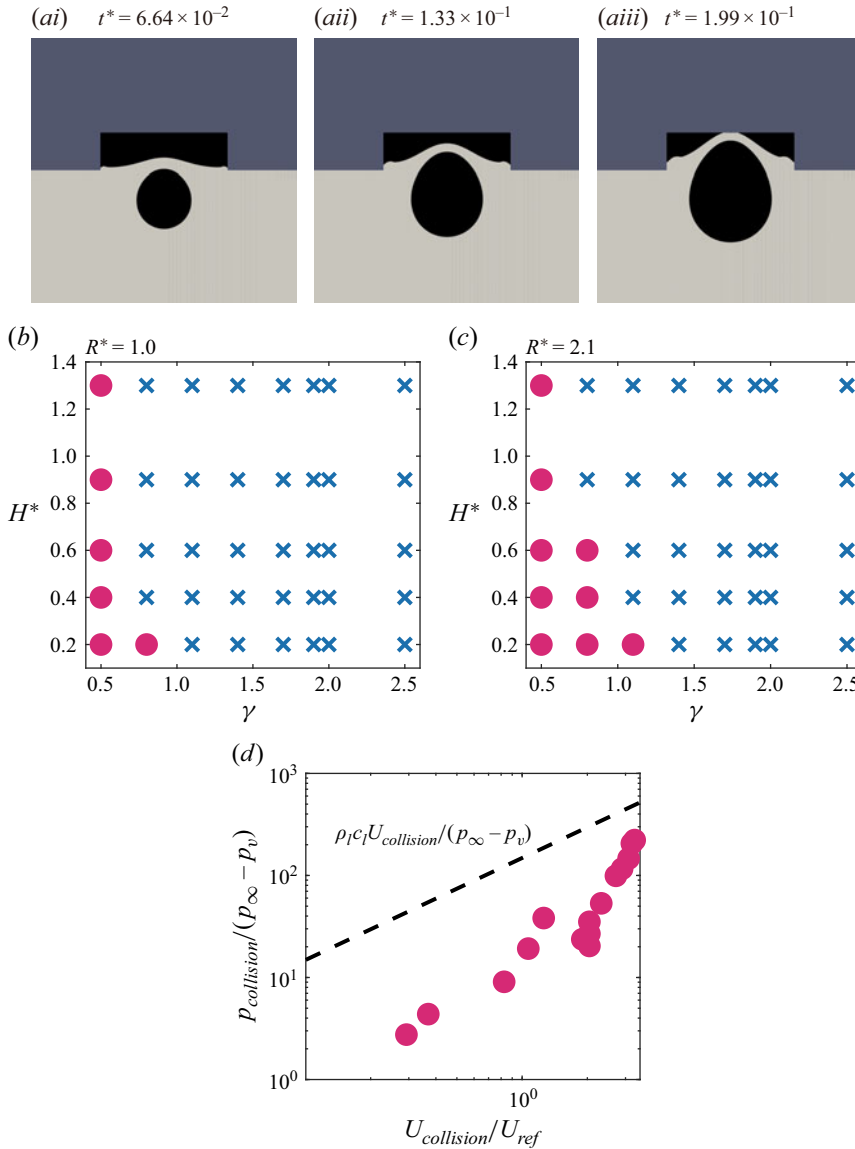


Figure 9. (a) Temporal evolution of water collision with the wall ($R^* = 1.0$, $H^* = 0.6$, $\gamma = 0.5$); see supplementary movie 2. Distribution of cases exhibiting water collision: (b) $R^* = 1.0$ and (c) $R^* = 2.1$. (d) Relation between maximum pressure $p_{collision}$ on the wall in the event of water collision and water collision speed $U_{collision}$. The purple circles denote cases where water collision occurs during bubble expansion. The pressure and speed in (d) are drawn on a logarithmic scale.

When a flat solid body impinges vertically on a free surface with collision speed $U_{collision}$, the pressure exerted on the flat body is estimated to be $\rho_l c_l U_{collision}$ from the simple water hammer model (Chuang 1966), and the pressure on the wall in our model can be estimated theoretically in the same manner. Here, ρ_l and c_l are the density and sound speed of the liquid. Although the compressibility of water is considered in our simulations, the change in water density is negligible; $\rho_l = 998 \text{ kg m}^{-3}$. From equation of state (2.1a), $c_l \approx c_\infty = 1477 \text{ m s}^{-1}$. Although the water hammer pressure $\rho_l c_l U_{collision}$ captures the

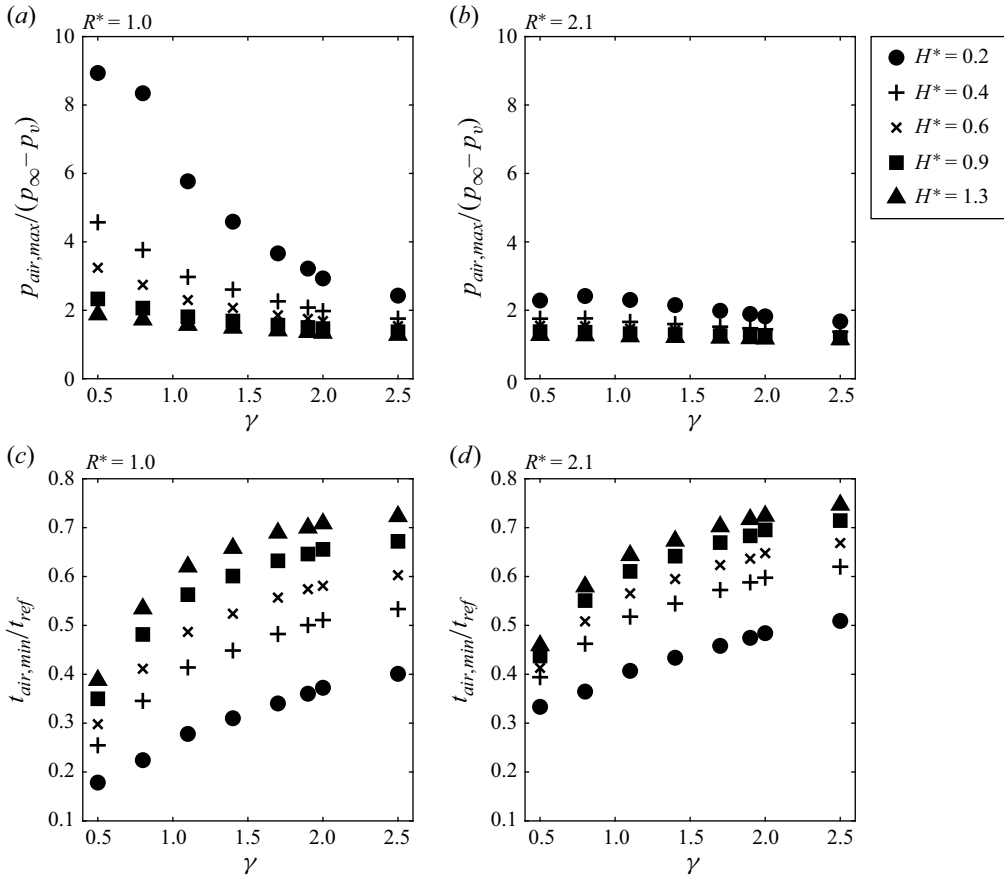


Figure 10. Maximum pressure of entrapped air, $p_{air,max}$, during air pocket contraction for (a) $R^* = 1.0$ and (b) $R^* = 2.1$. Rebound time of entrapped air, $t_{air,min}$, for (c) $R^* = 1.0$ and (d) $R^* = 2.1$.

trend of $p_{collision}$ with respect to $U_{collision}$ to some extent, it exceeds the actual value of $p_{collision}$ obtained from the simulations. This discrepancy arises because the assumptions used for the water hammer pressure model are violated in our water collision situation. While the water hammer pressure $\rho l c_l U_{collision}$ is estimated from the collision of a sufficient amount of water with a flat solid, only a thin film of water collides with the wall in our simulations (figure 9a). The existence of the entrapped air inside the pocket, which is not accounted for in the water hammer model, also reduces the actual collision pressure compared with the water hammer pressure.

The compression of the air in the pocket through bubble expansion leads to an increase in the volume-averaged pressure of the compressed air. Evidently, the growth rate of the air pressure decreases over time, and $p_{air,max}$ also decreases as the initial volume of air increases with larger R^* and H^* (figure 10a,b). As the initial volume of air has a linear relationship with R_p^2 and H_p , R^* has a greater influence on the change in air pressure than H^* . The upward movement of the water–air interface slows and eventually stops when the air volume is minimised. For small R^* and H^* , the air pressure increases rapidly during compression, and sequentially the air rebounds (expands) earlier from its most compressed state (figure 10c,d). In the figure, the rebound time of the air, $t_{air,min}$, is defined as the time at which the air volume reaches its minimum, which also marks the moment at which the air begins to expand. If the initial bubble is located farther away from the air pocket, then

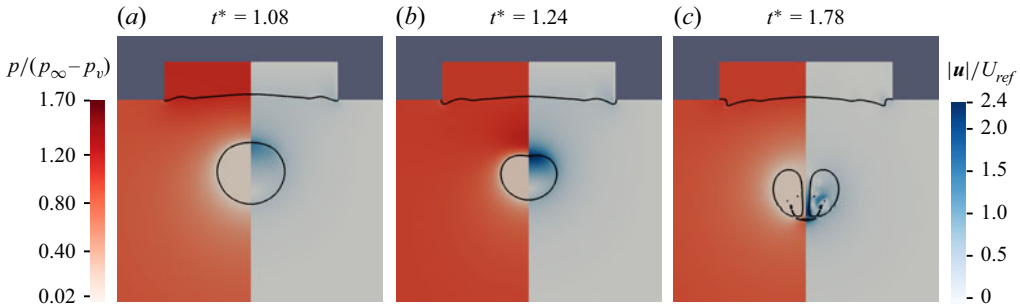


Figure 11. Formation of the bubble jet near the air pocket ($R^* = 2.1$, $H^* = 0.9$, $\gamma = 1.7$): pressure field (left) and velocity magnitude field (right).

the compression of the air by the bubble weakens. Accordingly, for a large value of γ , the maximum air pressure decreases, and the rebound of the air is delayed (figure 10). The rebound time of the air is related to the contraction of the upper interface of the bubble, which is explained in the next subsection.

3.3. Bubble contraction and air pocket expansion

After bubble expansion, the pressure within the bubble falls below that of its surroundings, leading to bubble contraction. A bubble jet is induced by the asymmetric contraction speed of the bubble interface. While a collapsing bubble near a rigid flat wall generates a bubble jet directed towards the wall (Lauterborn & Bolle 1975; Brujan *et al.* 2002; Tomita *et al.* 2002; Zhang *et al.* 2022), the direction of the bubble jet changes to the downward direction for most of the air pocket cases considered in this study (figure 11). The downward bubble jet occurs near the contracting upper interface of the bubble, and can eventually penetrate the bubble along the axisymmetric axis. However, for $R^* = 1.0$, the upper interface of the bubble does not penetrate the centre of the lower interface of the bubble in several cases ($[H^*, \gamma] = [0.2, 1.7-2.5]$, $[0.4-1.3, 1.7]$, $[0.6-1.3, 1.4]$). Although the conditions determining bubble penetration are not the focus of this study, penetration may be absent by the combined effects of the rigid wall and the entrapped air in the pocket.

The change in the bubble jet direction can be explained by considering the inertia of the air inside the pocket and the pressure distribution near the bubble, similar to the mechanism of bubble jet formation adjacent to a free surface (Robinson *et al.* 2001). The lower inertia of the air compared with the water causes the upper interface of the bubble, which is closer to the air pocket, to move faster than its lower interface. Therefore, the upper interface of the bubble curves outwards more with respect to the bubble centre during the stage of bubble expansion, and shrinks rapidly during the stage of bubble contraction. The rapid contraction of the upper interface is demonstrated on the right-hand side (velocity magnitude field) of figure 11(a). The contracting bubble pulls the surrounding water towards the bubble, and the pressure in the vicinity of the bubble increases. In particular, because the upper interface of the bubble contracts at a faster rate than the other interfaces, a region of higher pressure is generated above the bubble (figure 11b). After the formation of this high-pressure region, the accelerated downward motion of the upper interface gives rise to a high-speed bubble jet directed away from the air pocket (figure 11c). Naturally, when the pocket depth and radius are sufficiently small, the influence of the rigid boundary dominates that of the air pocket, leading to jet

formation towards the pocket instead. A detailed analysis of this transition is provided in [Appendix A](#).

Although the downward-moving bubble jet does not directly cause notable hydrodynamic loading on the wall, two representative properties of the collapsing bubble and bubble jet are briefly discussed: the speed of the bubble jet, and the collapse time of the bubble. In this study, the bubble jet speed U_{bubble} is defined as the speed of the centre on the upper interface of the bubble at the instant before it reaches the opposing lower interface; this is positive in the downward direction. If the upper interface of the bubble does not penetrate its lower interface, then the bubble jet speed is not defined. For most cases in which $\gamma > 1.0$, U_{bubble} tends to increase with increasing γ , although the initial bubble is located farther from the air pocket, which is similar to that observed in free-surface cases (Supponen *et al.* 2016). For $\gamma > 1.0$, the air pocket and the wall, which are responsible for inducing aspherical collapse, are located farther away from the bubble. Because of the reduction in the degree of anisotropy with increasing γ , the bubble jet accelerates for a longer duration, increasing its speed. Additionally, unlike typical free-surface cases, the presence of an air pocket introduces a unique effect; the compressed air pocket rebounds downwards, actively contributing to the contraction of the upper bubble interface. According to [figure 10\(c,d\)](#) of § 3.2, as H^* and γ increase, the rebound of the air pocket occurs at a later time. Consequently, the contraction of the upper bubble interface is also delayed, increasing the distance between the top-most and bottom-most points of the bubble at the onset of bubble contraction. The bubble jet should accelerate in the longer distance until it reaches the lower bubble interface. This extended acceleration time eventually leads to the increase in U_{bubble} for larger values of H^* and γ when $\gamma > 1.0$. This trend is consistently observed throughout our investigation range up to $\gamma = 2.5$.

However, the trend of U_{bubble} versus H^* and γ reverses when $\gamma < 1.0$ ([figure 12](#)). The non-monotonic trend of U_{bubble} with respect to γ is attributed to the fact that for $\gamma < 1.0$, the bubble jet speed is governed by mechanisms different from those described above. In this range, the expanding bubble aggressively intrudes into the region of the original air pocket, leading to the strongest contraction of the air in the pocket. Additionally, because γ is small, the distance between the bubble interface and the rebounding pocket interface is significantly reduced during the contraction phase of the bubble, which follows its maximum radial expansion. Consequently, the rebounding motion of the air pocket interface and the strong pressure field play a more direct role in bubble contraction and jet formation, resulting in a higher jet speed.

Next, we define the bubble collapse time $t_{collapse}$ as the period from the initial state to the start of the second bubble expansion, when the bubble has its minimum volume. A cavitation bubble near a flat wall collapses later than an unbounded bubble (Vogel, Lauterborn & Timm 1989; Lindau & Lauterborn 2003; Sun *et al.* 2022a). This result is attributed to the role of the wall as an obstacle that slows the flow in the upper region of the bubble, thereby delaying the bubble collapse (Li *et al.* 2019). By contrast, because the free surface enhances the motion of the bubble during its expansion and contraction in comparison to a flat wall, the bubble collapses faster when it is positioned closer to the air pocket with smaller γ ([figure 13](#)). As mentioned before, an air pocket with a large pocket depth begins to push the bubble at a relatively late time (i.e. with a greater rebound time $t_{air,min}$), and this delayed rebound (expansion) of the air pocket results in the delayed bubble collapse. That is, the rebound time of the air, $t_{air,min}$ in [figure 10\(c,d\)](#), is correlated with $t_{collapse}$ of the bubble in [figure 13](#), and both have monotonically increasing relations with H^* and γ .

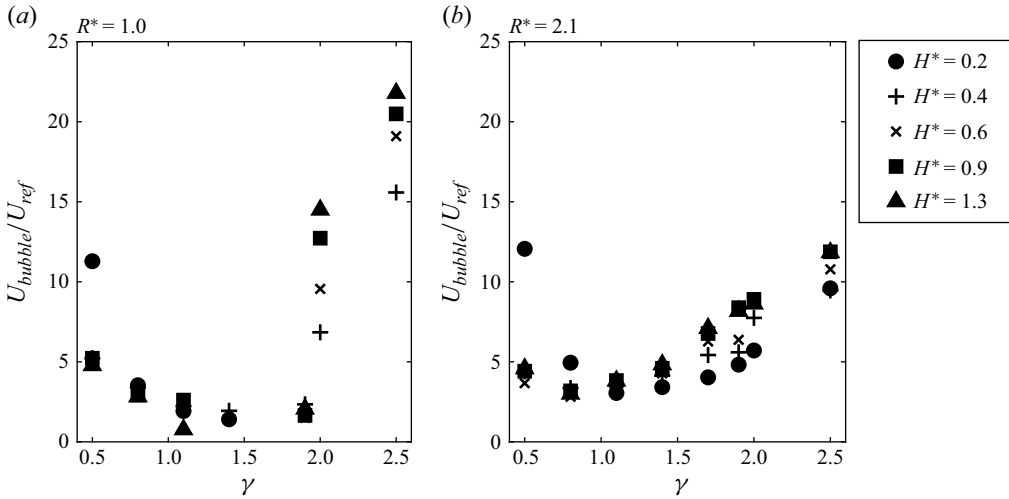


Figure 12. Bubble jet speed U_{bubble} for (a) $R^* = 1.0$ and (b) $R^* = 2.1$. Here, U_{bubble} is positive in the direction away from the air pocket.

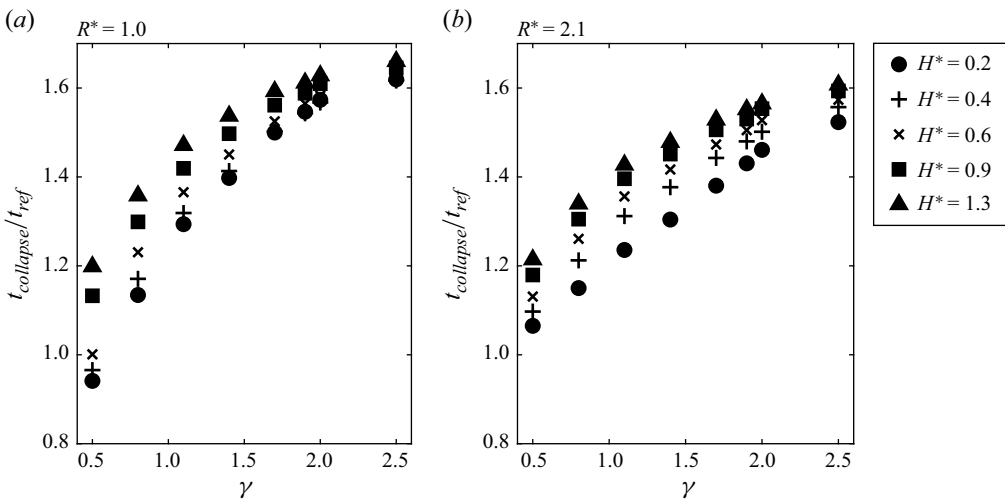


Figure 13. Bubble collapse time $t_{collapse}$ for (a) $R^* = 1.0$ and (b) $R^* = 2.1$.

3.4. Pocket jet formation

When the bubble undergoes its second expansion after the collapse, a notable phenomenon occurs in the air pocket – an upward liquid jet is created at the water–air interface of the pocket (see [figure 14](#) and supplementary movie 3). We refer to this as a pocket jet. The formation of the pocket jet is the most distinct feature in the dynamics of entrapped air through the entire cycle. The pocket jet does not occur when $\gamma < 1.0$ because the water–air interface collides with the ceiling of the pocket ([figure 9b,c](#)). Therefore, only the cases for which $\gamma > 1.0$ are considered in this subsection.

The pocket jet can be categorised as either a central pocket jet or a lateral pocket jet, depending on its origin. The central pocket jet forms at the central axis of the pocket ([figure 14a,b](#)). If the central pocket jet moves upwards and reaches the ceiling inside the air pocket, then it exerts significant pressure on the wall ([figure 14a,c](#)). [Duy *et al.* \(2023\)](#)

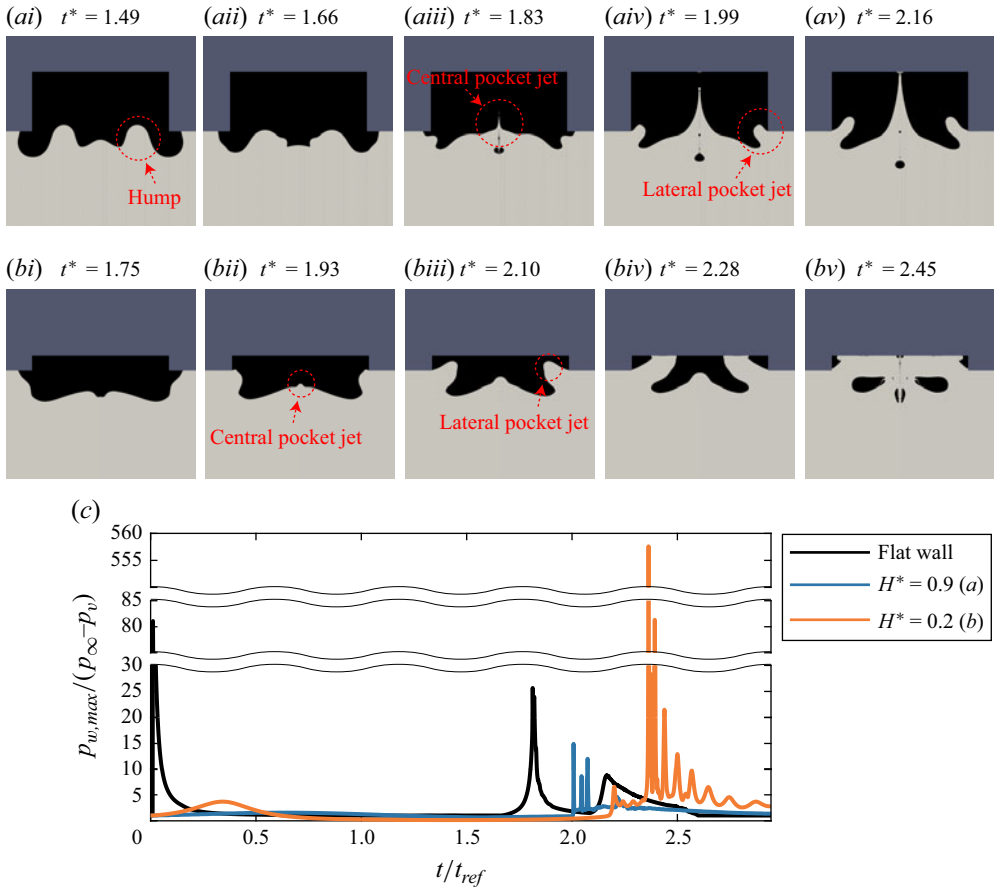


Figure 14. Temporal evolution of the water–air interface and formation of the pocket jet during the second air pocket contraction for (a) $R^* = 1.0$, $H^* = 0.9$, $\gamma = 1.7$ and (b) $R^* = 1.0$, $H^* = 0.2$, $\gamma = 1.7$; see supplementary movie 3. (c) Time histories of maximum pressure on the wall, $p_{w,max}$, for the two cases in (a) and (b), and the flat wall case ($\gamma = 1.7$). The pressure is drawn on a logarithmic scale.

observed that when a bubble was generated near a hole filled with air, a jet propagated upwards through the water–air interface to a depth more than three times the maximum radius of the bubble. In their study, the depth of the hole was sufficient to prevent the jet from impacting the wall. However, in the present study, the central pocket jet can impact the wall because the size of the air pocket is similar to the maximum radius of the bubble. In figure 15(a), $p_{w,cen}$ is the maximum pressure on the wall from the impact of the central pocket jet. We see that $p_{w,cen}$ can reach 40 times the atmospheric pressure. Nevertheless, in most cases, $p_{w,cen}$ is less than the pressure generated by a bubble jet (directed towards the wall) in the flat wall cases (bar symbols in figure 15a,b). For $H^* = 0.2$, the central pocket jet does not reach the wall because it is interrupted by a lateral pocket jet, which is why no data are available for these cases in figure 15(a). The $\gamma = 2.5$ cases are also absent from figure 15(a) because the central pocket jet is either entirely interrupted by the lateral pocket jet or too slow to reach the wall during the simulation time.

The lateral pocket jet is generated at the circumferential edge of the air pocket entrance after bubble collapse, and propagates inwards (figure 14a,b). In the case of small H^* (e.g. $H^* = 0.2$), the lateral pocket jet impacts the wall, although the pressure that it exerts

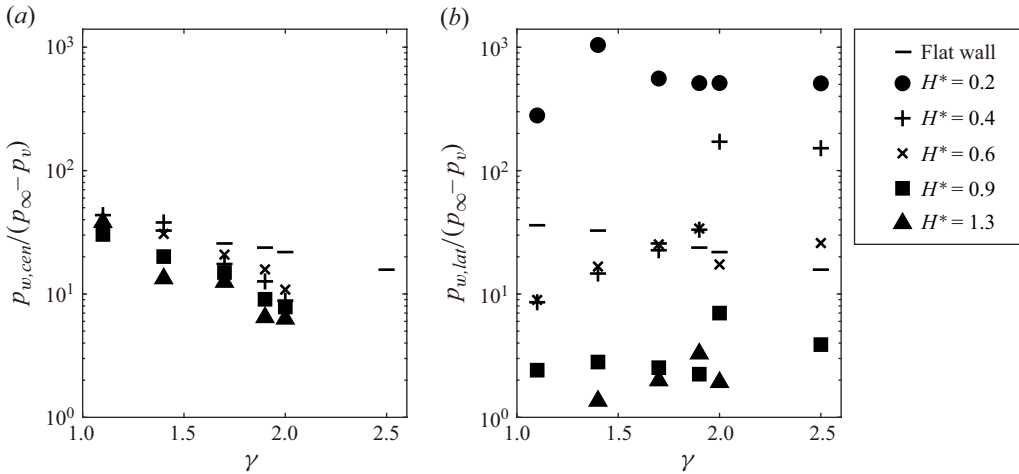


Figure 15. (a) Maximum pressure on the wall induced by the central pocket jet, $p_{w,cen}$, and (b) maximum pressure on the wall induced by the lateral pocket jet, $p_{w,lat}$, for $R^* = 1.0$. The pressure is drawn on a logarithmic scale.

is only several times the atmospheric pressure (figure 14b,c). After the lateral pocket jet impacts the wall, it moves inwards and converges at the centre of the pocket wall, creating a strong vertical momentum along the z -axis. In this scenario, the central pocket jet cannot reach the pocket wall because of interference by the lateral pocket jet, and the pressure resulting from the vertical momentum of the converged lateral pocket jet is much greater than the pressure caused by the initial impact of the lateral pocket jet. The maximum pressure induced by the lateral pocket jet, $p_{w,lat}$, can be several hundred times the atmospheric pressure, even exceeding the pressure induced by a bubble jet in the flat wall cases (figures 14(c) and 15(b)). That is, if the ceiling of the air pocket is quite low, then the air pocket can have negative effects on the hydrodynamic loading on the wall because the converged lateral pocket jet induces a significant vertical spread. If the lateral pocket jet does not reach the wall due to blockage by the central pocket jet, then the lateral pocket jet cannot impose a high pressure on the wall. The sequential order in which the lateral pocket jet and the central pocket jet reach the wall, and their interaction, are a complex function of input parameters such as H^* and γ . Thus the interaction of the two pocket jets is not analysed in this study.

To elucidate the effects of each of the two pocket jets on the wall pressure, their formation and dynamics should be examined in detail. The formation of the central pocket jet is relevant to the radially moving hump at the water–air interface, which appears during the first bubble expansion. For this reason, we first discuss the mechanism of hump formation at the water–air interface. At the beginning of the first bubble expansion, the surrounding water is pushed radially outwards due to the expansion. However, the movement of the water above the bubble is constrained by the presence of the wall (figure 16a). A portion of the water begins to intrude into the air pocket, which first occurs at the circumferential edge where the wall meets the pocket ($t^* = 0.02$ in figure 16b). This intrusion leads to the formation of a hump near the edge, and the hump continues to amplify as more water rushes in as time advances. When the bubble reaches its maximum radius and begins to contract ($t^* = 0.67$ in figure 16b), the hump starts to propagate along the water–air interface towards the centre of the pocket. At this instant, the velocity of water near the water–air interface reverses its direction towards the bubble.

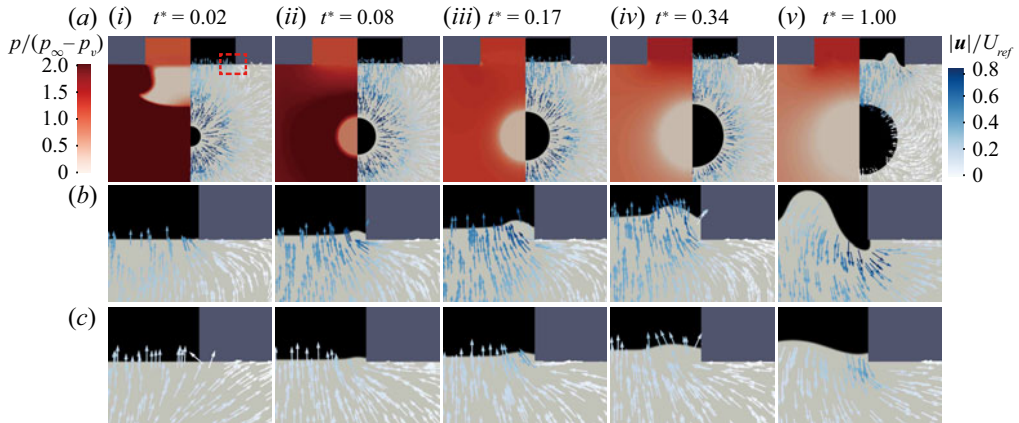


Figure 16. (a) Temporal evolution of pressure (left) and velocity (right) fields around the bubble and air pocket up to the beginning of the bubble contraction phase ($R^* = 1.0$, $H^* = 0.6$, $\gamma = 1.6$). Magnified images of the region indicated by the red dashed line in (a): (b) $R^* = 1.0$ and (c) $R^* = 2.1$ ($H^* = 0.6$, $\gamma = 1.6$).

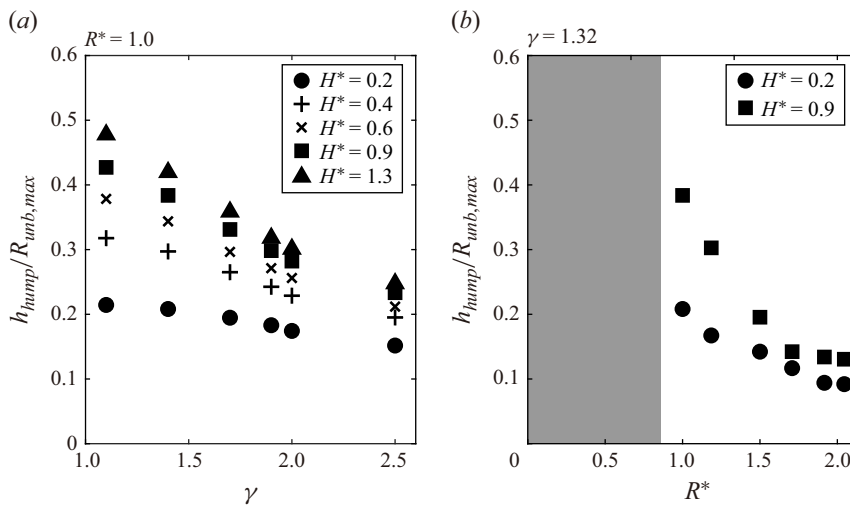


Figure 17. (a) Effect of γ and H^* on maximum vertical displacement of the hump, h_{hump} ($R^* = 1.0$). (b) Effect of R^* on h_{hump} ($H^* = [0.2, 0.9]$ and $\gamma = 1.32$). The grey area denotes the conditions in which a hump collides directly with the ceiling inside the pocket.

The height of the hump, h_{hump} , is determined by the amount of water pushed away by the bubble expansion and intruded into the pocket near the circumferential edge. Here, h_{hump} is defined as the maximum vertical displacement of the top-most point of the hump from the initial horizontal water–air interface; h_{hump} decreases with increasing γ (figure 17a), because the effect of the bubble on the hump weakens as the distance between the bubble and the pocket edge increases. Furthermore, the increase in H^* enlarges the initial volume of entrapped air, which enables the sufficient compression of the air. This allows a greater amount of water to flow into the pocket and contribute to the increase in h_{hump} .

To examine the effect of R^* on h_{hump} , additional simulations are conducted by varying $R^* = 0.2$ – 2.1 for $H^* = [0.2, 0.9]$ and $\gamma = 1.32$. When R^* is relatively small (e.g.

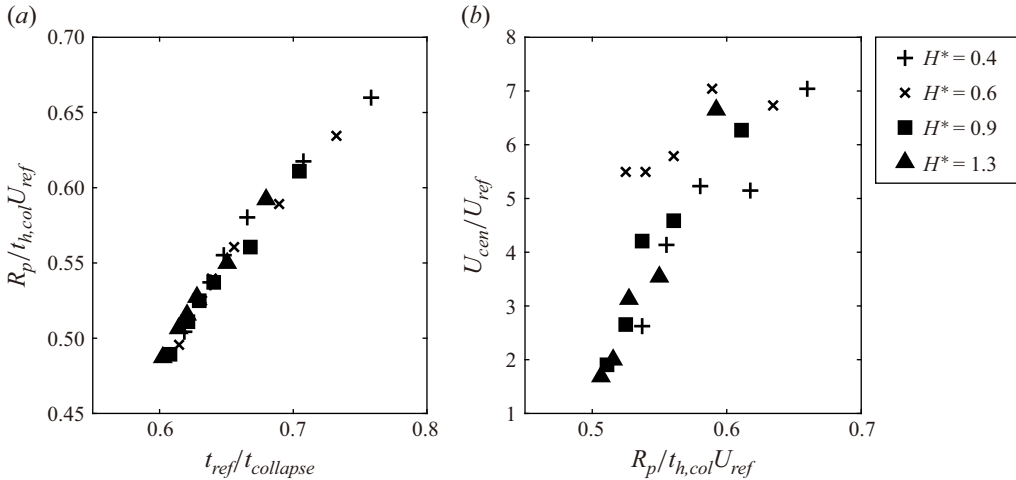


Figure 18. (a) Radial hump speed $R_p/t_{h,col}$ versus the inverse of bubble collapse time $1/t_{collapse}$, and (b) central pocket jet speed U_{cen} versus $R_p/t_{h,col}$, for $R^* = 1.0$. Cases in which the central pocket jet does not reach the wall are omitted from (a) and (b).

$R^* = 1.0$), water is pushed away by the bubble and then deflected into the pocket by the wall (figure 16b). However, when R^* increases, the angle of the line connecting the bubble centre and the pocket edge with respect to the z -axis becomes greater even for the same γ , leading to a greater radial component in the flow field around the pocket edge. Thus the amount of water flowing into the pocket declines, and h_{hump} becomes smaller with R^* (figure 17b); also compare the $R^* = 1.0$ and $R^* = 2.1$ cases in figure 16(b,c). Additionally, the increased absolute distance from the bubble to the pocket edge weakens the induced flow of water, further contributing to the decrease in h_{hump} . On the other hand, when R^* is below 0.8, the hump strengthens and directly reaches the ceiling inside the pocket before forming a distinct peak, such that h_{hump} cannot be defined. The origin of the central pocket jet is the concentrated momentum at the central axis of the pocket, which is created by the radially inward motion of the hump. Because h_{hump} is much smaller in the cases for $R^* = 2.1$ compared to $R^* = 1.0$ (figure 17b), the concentrated momentum is not strong enough to create a central pocket jet, and a central pocket jet is not observed in any case for $R^* = 2.1$.

The dominant driving force acting on the hump is the pressure gradient in the water, which is attributable to the high (or low) pressure inside the bubble. The radial propagation speed of the hump is approximated as $R_p/t_{h,col}$, where R_p is the air pocket radius, and $t_{h,col}$ is the instant at which the humps collide with each other at the central axis of the air pocket. According to figure 18(a), this hump speed is linearly related to $1/t_{collapse}$, which indicates the oscillation frequency of the bubble; see figure 13 in § 3.3 for $t_{collapse}$. This linear relation exists because the fluctuation of the hump is synchronised with the expansion and collapse of the bubble.

The radially moving hump is converged at the central axis of the pocket, causing the formation of a central pocket jet moving upwards, as depicted in figure 14(a_{iii}–a_v). The speed of the central pocket jet, U_{cen} , is defined as the vertical speed of the jet tip or the droplets separated from the jet at the time step immediately before they reach the ceiling of the pocket. Because several droplets can separate from the jet, the jet tip or droplet that exerts the highest pressure on the wall is chosen to define U_{cen} . The vertical speed of the central pocket jet has an approximately linear relation with the radial speed of the

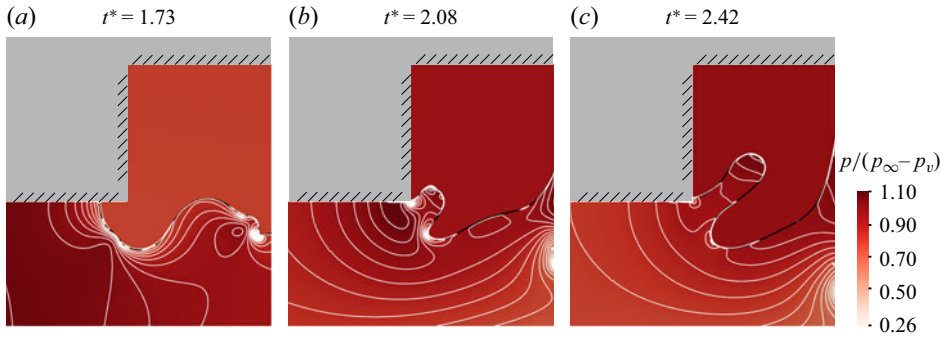


Figure 19. Pressure distribution during the formation of the lateral pocket jet ($R^* = 1.0$, $H^* = 0.9$, $\gamma = 1.7$). The black and white lines denote the water–air interface and the isocontours of pressure in the water, respectively.

hump, $R_p/t_{h,col}$ (figure 18*b*). In figure 18(*a,b*), the collapse time $t_{collapse}$ of the bubble is inversely related to the impact speed U_{cen} of the central pocket jet. This result highlights that the dynamics of the bubble in the previous stages affects the strength of the central pocket jet.

After the generation of the hump, a lateral pocket jet typically forms near the edge of the pocket entrance during the second contraction of the air, as depicted in figure 14. Although both the contracting air inside the pocket and the expanding bubble can affect the formation process of the lateral pocket jet, the effect of the bubble rapidly weakens because of the relative position of the lateral pocket jet. In figure 19, the inward-moving lateral pocket jet is eventually above the engulfed air region, and the engulfed air region prevents the pressure-gradient force caused by the expanding bubble from influencing the dynamics of the lateral pocket jet. While the pressure gradient is pronounced in the normal direction near a gently deformed water–air interface (figure 19*a*), it is less significant in figure 19(*c*) at the instant when the lateral pocket jet is positioned above the air. That is, the propagation speed of the lateral pocket jet is determined primarily by the contraction of the air, rather than the expansion of the bubble.

To examine the effect of air pocket contraction on the lateral pocket jet, the change in the potential energy of the entrapped air, ΔE_{air} , is calculated as (Wang 2016)

$$\Delta E_{air} = (p_{\infty} - p_v)(V_{air,1} - V_{air,2}) + \frac{p_{\infty} V_{air,0}}{\kappa - 1} \left[\left(\frac{V_{air,0}}{V_{air,1}} \right)^{\kappa-1} - \left(\frac{V_{air,0}}{V_{air,2}} \right)^{\kappa-1} \right]. \quad (3.1)$$

The change in potential energy due to variations in surface tension and gravity is negligible, and these terms are omitted in (3.1). Here, $V_{air,1}$ indicates the volume of air at the instant when it attains a maximum (i.e. at the start of the second air contraction). The air volume $V_{air,2}$ is obtained after a certain dimensionless time $\Delta t^* = 0.52$ passes from the instant corresponding to $V_{air,1}$. Later, we attempt to determine how the change in the potential energy of the entrapped air is related to the change in the kinetic energy of the lateral pocket jet between the two specific instants (with subscripts 1 and 2). Except for one case ($H^* = 0.2$, $\gamma = 1.1$), the lateral pocket jet does not reach the wall or interfere with another water–air interface until $\Delta t^* = 0.52$ after the instant corresponding to $V_{air,1}$; thus the case $H^* = 0.2$ and $\gamma = 1.1$ is excluded from this energy analysis and figure 21 below. To evaluate the kinetic energy of the lateral pocket jet before its collision with the

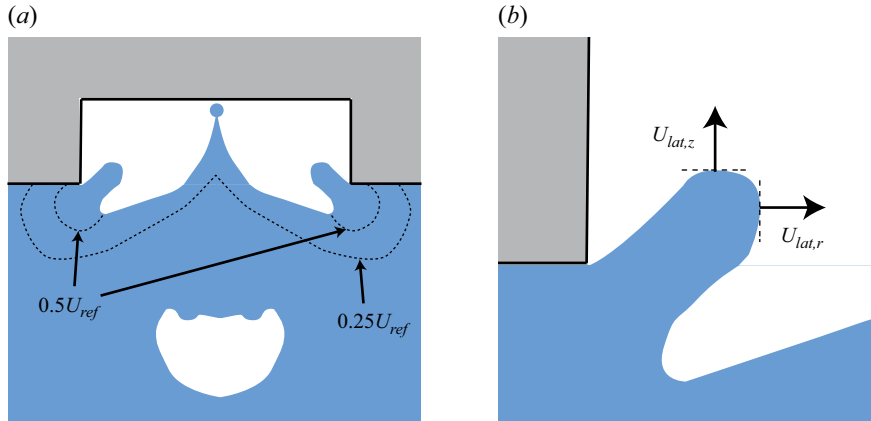


Figure 20. (a) Schematic of lateral pocket jet boundaries with different threshold values ($0.25U_{ref}$ and $0.5U_{ref}$). (b) Definition of radial and axial velocity components $U_{lat,r}$ and $U_{lat,z}$ for the lateral pocket jet.

wall or the central pocket jet, $\Delta t^* = 0.52$ between instants 1 and 2 is adopted consistently for all cases.

During the second air contraction, some of the potential energy of the air is converted into the kinetic energy of the lateral pocket jet. To estimate the kinetic energy of the lateral pocket jet, the threshold speed of water is first determined for the boundary of the lateral pocket jet (figure 20a). If the threshold speed is too low (e.g. $0.25U_{ref}$), then the central and lateral pocket jets cannot be distinguished. Conversely, no lateral pocket jet can be detected if the threshold speed is too high. Therefore, the threshold speed is set to an arbitrary value of $0.5U_{ref}$ ($= 4.98 \text{ m s}^{-1}$) such that a reasonable region of water is considered as a lateral pocket jet. The change in the kinetic energy of the lateral pocket jet between the two instants corresponding to $V_{air,1}$ and $V_{air,2}$ in (3.1) is then computed from

$$\Delta E_{k,lat} = \int_{V_{lat}} \frac{1}{2} \rho |\mathbf{u}|^2 dV, \quad (3.2)$$

where V_{lat} is the volume of the lateral pocket jet at the instant corresponding to $V_{air,2}$. The kinetic energy is negligible at the start of the second air contraction, $V_{air,1}$. We define the characteristic speed of the lateral pocket jet as $U_{lat} = (U_{lat,r}^2 + U_{lat,z}^2)^{1/2}$, where $U_{lat,r}$ ($U_{lat,z}$) is the radial (axial) velocity component measured at the radially innermost (axially uppermost) point of the water–air interface (figure 20b).

In figure 21(a), the change in the dimensionless kinetic energy of the lateral pocket jet, $\Delta E_{k,lat}/p_{\infty} V_{air,0}$, is proportional to the change in the dimensionless potential energy of the air, $\Delta E_{air}/p_{\infty} V_{air,0}$, and these quantities have similar magnitudes. This suggests that the kinetic energy of the lateral pocket jet primarily originates from the potential energy of the air. Furthermore, $\Delta E_{k,lat}/p_{\infty} V_{air,0}$ scales approximately as $(U_{lat}/U_{ref})^{3.5}$, rather than $(U_{lat}/U_{ref})^2$ (figure 21b); the exponent 3.5 is determined by the least squares method. This scaling is a result of the characteristic speed U_{lat} not accurately reflecting the distribution of the speed in the entire region of the lateral pocket jet from an energy perspective. Nevertheless, the strong correlation between the kinetic energy difference and speed of the lateral pocket jet can be derived from our definition of U_{lat} .

As reported in figure 15(b), the lateral pocket jet imparts a significant pressure on the wall when it converges at the central axis of the pocket for $H^* = 0.2$ and in the large- γ cases for $H^* = 0.4$ ($\gamma = 2.0-2.5$), but imparts only a minor pressure for $H^* = 0.9$ and 1.3.

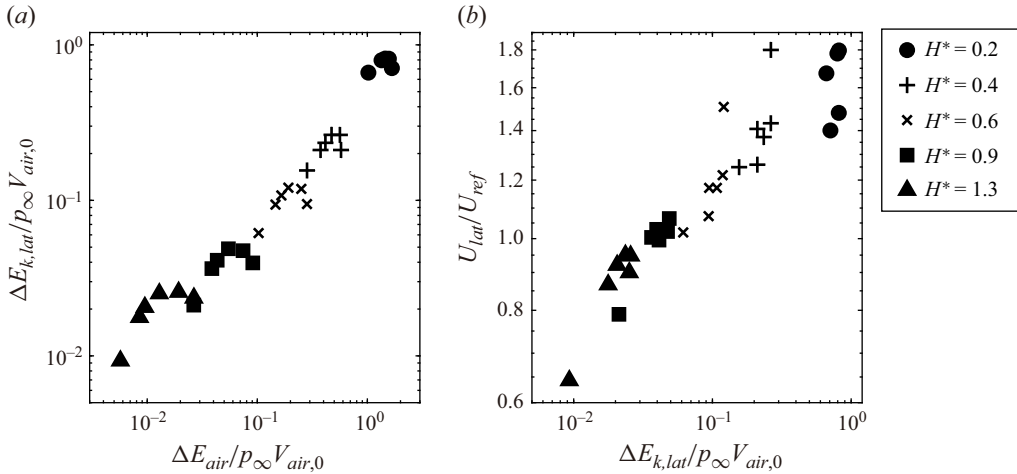


Figure 21. (a) Change in the dimensionless kinetic energy of the lateral pocket jet, $\Delta E_{k,lat}/p_{\infty}V_{air,0}$, versus change in the dimensionless potential energy of the air, $\Delta E_{air}/p_{\infty}V_{air,0}$, and (b) dimensionless speed of the lateral pocket jet, U_{lat}/U_{ref} , versus $\Delta E_{k,lat}/p_{\infty}V_{air,0}$, for $R^* = 1.0$. All variables are drawn on a logarithmic scale.

This trend is correlated with the results in figure 21. Although the kinetic energy of the lateral pocket jet, $\Delta E_{k,lat}$, in figure 21 is made dimensionless by $p_{\infty}V_{air,0}$ to account for the effect of the initial volume $V_{air,0}$ of the air pocket (i.e. the effect of H^* ; $V_{air,0} \sim H_p$), the dimensional $\Delta E_{k,lat}$ itself, in addition to $\Delta E_{k,lat}/p_{\infty}V_{air,0}$, is greater for $H^* = 0.2$ than for other values of H^* , and is inversely related to H^* for a given γ . The characteristic speed of the lateral pocket jet, U_{lat} , also shows the same trend in terms of H^* , suggesting the production of strong hydrodynamic loading on the wall for $H^* = 0.2$.

When the pocket radius R^* increases, the relative height of the water–air interface that can be pulled up decreases because the perimeter of the pocket extends. The lateral pocket jet does not develop sufficiently to extend above the air, but instead disappears during the fluctuation of the water–air interface. Accordingly, no lateral pocket jets can be clearly observed for $R^* = 2.1$. The effect of R^* on the formation of the lateral pocket jet can also be explained using the dimensionless energies and speed of the lateral pocket jet from the data for $R^* = 1.0$ in figure 21. Because $V_{air,0} \sim R_p^2$, and ΔE_{air} is relatively small for larger R^* , the dimensionless potential energy difference of the air, $\Delta E_{air}/p_{\infty}V_{air,0}$, decreases significantly for larger R^* . As a result, the dimensionless kinetic energy difference $\Delta E_{k,lat}/p_{\infty}V_{air,0}$ and the lateral pocket jet speed U_{lat}/U_{ref} are expected to decrease significantly as R^* increases, as shown in figure 21.

In summary, the trends of maximum pressure on the wall induced by the central or lateral pocket jet ($p_{w, cen}$ and $p_{w, lat}$ in figure 15) with respect to H^* agree with those of the central or lateral pocket jet speed (U_{cen} in figure 18(b) and U_{lat} in figure 21(b)). As H^* increases, $p_{w, cen}$ and $p_{w, lat}$ tend to decrease, and a similar trend is observed in U_{cen} and U_{lat} . In general, U_{cen} exceeds U_{lat} for large H^* (e.g. $H^* = 0.9, 1.3$), thus the central pocket jet prevents the convergence of the lateral pocket jet at the central axis of the pocket, annihilating the influence of the lateral pocket jet on hydrodynamic loading. By contrast, for small H^* (e.g. $H^* = 0.2$), the lateral pocket jet becomes prevalent with a higher speed, while the central pocket jet does not develop distinctly, which eventually yields strong convergence of the lateral pocket jet at the central axis, and significant hydrodynamic loading.

4. Concluding remarks

We have examined the hydrodynamic loading on a nearby wall caused by a cavitation bubble in the presence of an air pocket. Specifically, we have focused on the interaction between the air pocket and the bubble. Compared with a flat wall, the maximum pressure on a wall with an air pocket is substantially lower during the first bubble expansion. When the bubble begins to expand, a shock wave propagates from the bubble and reflects at the water–air interface of the air pocket, leading to remarkable mitigation of the hydrodynamic loading on the wall. If the bubble is located close to the water–air interface and the pocket is too shallow, then the water collides with the wall directly, resulting in high pressure on the wall despite the presence of the air pocket. The contraction of the air in the pocket caused by the expansion of the bubble affects the temporal evolution of the bubble in the next stage of bubble contraction. In contrast to the case without the air pocket, the bubble jet is directed away from the wall when the air pocket is present, thereby reducing the risk of cavitation erosion. Because of the low inertia of the air in the pocket, the bubble interface facing the air pocket expands and contracts faster than the other interface of the bubble, causing a change in the bubble jet direction. Importantly, even after the bubble collapse, significant pressure comparable to that of the bubble jet impinging on the flat wall can be produced on the wall. This can be attributed to central and lateral pocket jets. The central pocket jet originates from momentum concentration by the radial motion of the hump formed at the water–air interface, the formation and radial motion of which are synchronised with the expansion and contraction of the bubble. By contrast, the lateral pocket jet is primarily induced by the second contraction of the entrapped air, because the potential energy of the air is converted to the kinetic energy of the lateral pocket jet. In cases with a large pocket radius, neither the central nor the lateral pocket jet develops sufficiently to impose hydrodynamic loading on the wall. For the central pocket jet, this is because of the large angle and distance between the pocket edge and the bubble, and for the lateral pocket jet, the lower magnitude of the change in the dimensionless potential energy of the air is responsible for the insufficient development.

In this study, we have only considered axisymmetric configurations of the cylindrical air pocket and the bubble. While this simplified model provides useful insights into the complex interactions between the entrapped air and the bubble, the asymmetric alignment of the air pocket and the bubble is essential for more realistic applications, and may reveal totally different behaviours. Future studies should also explore a wider range of air pocket size, as well as various shapes and material properties of the pocket, to comprehensively examine the coupled dynamics in sequential stages, and identify the optimal model in terms of alleviating hydrodynamic loading.

Supplementary movies. Supplementary movies are available at <https://doi.org/10.1017/jfm.2025.10398>.

Funding. This work was supported by a National Research Foundation of Korea grant funded by the Korean government (MSIT) (RS-2024-00355146).

Declaration of interests. The authors report no conflict of interest.

Appendix A. Transition of bubble jet direction by change in air pocket size

In this study, the size of the air pocket is limited to $R^* = [1.0, 2.1]$ and $H^* = 0.2\text{--}1.3$. Under these conditions, the bubble jet consistently propagates in the direction opposite to the air pocket in most cases. However, when R^* and H^* are sufficiently small, the influence of the nearby rigid solid boundary becomes more dominant than that of the air pocket. Consequently, due to the well-known characteristics of the rigid solid boundary,

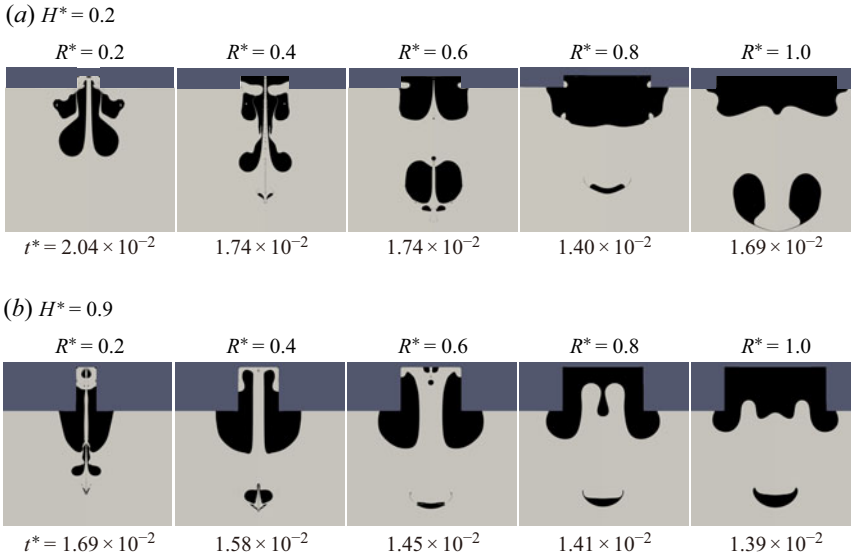


Figure 22. Change in bubble jet direction by R^* : (a) $H^* = 0.2$ and (b) $H^* = 0.9$.

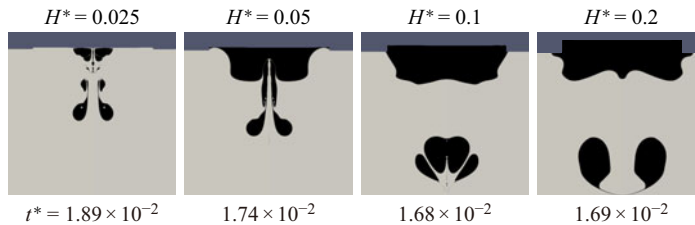


Figure 23. Change in bubble jet direction by H^* for very shallow pocket depths ($R^* = 1.0$).

the bubble jet is expected to be directed towards the pocket. To identify the existence of the threshold values of R^* and H^* at which this directional transition occurs, additional simulations are conducted for $\gamma = 1.32$. First, to examine the influence of R^* , it is varied as $R^* = 0.2$ – 1.0 while maintaining $H^* = [0.2, 0.9]$, and the resulting bubble jet direction is analysed. For $H^* = 0.2$, the jet consistently forms in the direction opposite to the air pocket when $R^* \geq 0.8$. For intermediate values of $R^* = [0.4, 0.6]$, however, the jet splits into the upward and downward components. For the smaller value $R^* = 0.2$, the bubble jet is fully directed towards the pocket. Similarly, for $H^* = 0.9$, the onset of jet splitting is observed when R^* is reduced to 0.4 or below (figure 22*b*). For $R^* \leq 0.4$, a split jet is initially developed, but most of its momentum is concentrated to the upward component.

Additionally, simulations are conducted by decreasing H^* below 0.2, while fixing $R^* = 1.0$: $H^* = [0.025, 0.05, 0.1]$ (figure 23). For $H^* = 0.1$, the bubble jet exhibits a splitting phenomenon in both upward and downward directions. However, the momentum directed towards the pocket is not strong enough to penetrate through the upper interface of the bubble. In the cases $H^* = 0.025$ and 0.05, the bubble jet is fully directed towards the pocket.

These findings indicate that when R^* or H^* becomes too small, the bubble jet tends to propagate towards the air pocket, momentarily disrupting the water–air interface. In such

cases, the interactions between the collapsing bubble and the air pocket differ significantly from those discussed in this study. The air pocket fails to redirect the bubble jet in the opposite direction to the boundary, and is unable to mitigate the wall pressure.

REFERENCES

- ABBONDANZA, D., GALLO, M. & CASCIOLA, C.M. 2024 Collapse of microbubbles over an elastoplastic wall. *J. Fluid Mech.* **999**, A72.
- ANDREWS, E.D., RIVAS, D.F. & PETERS, I.R. 2023 Bubble collapse near porous plates. *J. Fluid Mech.* **962**, A11.
- BHOLA, S.Jr, RODRIGUEZ, M., BEIG, S.A., BARBIER, C.N. & JOHNSEN, E. 2025 Inertial collapse of a gas bubble in a shear flow near a rigid wall. *J. Fluid Mech.* **1004**, A3.
- BLAKE, J.R. & GIBSON, D.C. 1981 Growth and collapse of a vapour cavity near a free surface. *J. Fluid Mech.* **111**, 123–140.
- BRACKBILL, J.U., KOTHE, D.B. & ZEMACH, C. 1992 A continuum method for modeling surface tension. *J. Comput. Phys.* **100** (2), 335–354.
- BRUJAN, E.A., KEEN, G.S., VOGEL, A. & BLAKE, J.R. 2002 The final stage of the collapse of a cavitation bubble close to a rigid boundary. *Phys. Fluids* **14** (1), 85–92.
- BRUJAN, E.A., NAHEN, K., SCHMIDT, P. & VOGEL, A. 2001a Dynamics of laser-induced cavitation bubbles near an elastic boundary. *J. Fluid Mech.* **433**, 251–281.
- BRUJAN, E.A., NAHEN, K., SCHMIDT, P. & VOGEL, A. 2001b Dynamics of laser-induced cavitation bubbles near elastic boundaries: influence of the elastic modulus. *J. Fluid Mech.* **433**, 283–314.
- BRUJAN, E.A., NODA, T., ISHIGAMI, A., OGASAWARA, T. & TAKAHIRA, H. 2018 Dynamics of laser-induced cavitation bubbles near two perpendicular rigid walls. *J. Fluid Mech.* **841**, 28–49.
- CHUANG, S.-L. 1966 Experiments on flat-bottom slamming. *J. Ship. Res.* **10** (1), 10–17.
- DUY, T.-N., NGUYEN, V.-T., PHAN, T.-H., NGUYEN, Q.-T., PARK, S.-H. & PARK, W.-G. 2023 Numerical study of bubble dynamics near a solid wall with a gas-entrapping hole. *Ocean Engng* **285**, 115344.
- GÁLVEZ, L.O., FRATERS, A., OFFERHAUS, H.L., VERSLUIS, M., HUNTER, I.W. & RIVAS, D.F. 2020 Microfluidics control the ballistic energy of thermocavitation liquid jets for needle-free injections. *J. Appl. Phys.* **127** (10), 104901.
- GILMORE, F.R. 1952 *The growth or collapse of a spherical bubble in a viscous compressible liquid* (vol. 26). Pasadena, CA: California Institute of Technology.
- GONZALEZ-AVILA, S.R., NGUYEN, D.M., ARUNACHALAM, S., DOMINGUES, E.M., MISHRA, H. & OHL, C.-D. 2020 Mitigating cavitation erosion using biomimetic gas-entrapping microtextured surfaces (GEMS). *Sci. Adv.* **6** (13), eaax6192.
- HAN, R., ZHANG, A.-M., TAN, S. & LI, S. 2022 Interaction of cavitation bubbles with the interface of two immiscible fluids on multiple time scales. *J. Fluid Mech.* **932**, A8.
- HORVAT, D., AGREŽ, V., POŽAR, T., STARMAN, B., HALILOVIĆ, M. & PETKOVŠEK, R. 2022 Laser-induced shock-wave-expanded nanobubbles in spherical geometry. *Ultrason. Sonochem.* **89**, 106160.
- ISSA, R.I. 1986 Solution of the implicitly discretised fluid flow equations by operator-splitting. *J. Comput. Phys.* **62** (1), 40–65.
- JIN, N., ZHANG, F., CUI, Y., SUN, L., GAO, H., PU, Z. & YANG, W. 2022 Environment-friendly surface cleaning using micro-nano bubbles. *Particuology* **66**, 1–9.
- KALAITZIS, A., MAKRYGIANNI, M., THEODORAKOS, I., HATZIAPOSTOULOU, A., MELAMED, S., KABLA, A., DE LA VEGA, F. & ZERGOTI, I. 2019 Jetting dynamics of Newtonian and non-Newtonian fluids via laser-induced forward transfer: experimental and simulation studies. *Appl. Surf. Sci.* **465**, 136–142.
- KIM, D. & KIM, D. 2020 Underwater bubble collapse on a ridge-patterned structure. *Phys. Fluids* **32** (5), 053312.
- KOBAYASHI, K., NAGAYAMA, T., WATANABE, M., FUJII, H. & KON, M. 2018 Molecular gas dynamics analysis on condensation coefficient of vapour during gas–vapour bubble collapse. *J. Fluid Mech.* **856**, 1045–1063.
- KOCH, M., LECHNER, C., REUTER, F., KÖHLER, K., METTIN, R. & LAUTERBORN, W. 2016 Numerical modeling of laser generated cavitation bubbles with the finite volume and volume of fluid method, using OpenFOAM. *Comput. Fluids* **126**, 71–90.
- KOUKOUVINIS, P., GAVAISES, M., SUPPONEN, O. & FARHAT, M. 2016 Simulation of bubble expansion and collapse in the vicinity of a free surface. *Phys. Fluids* **28** (5), 052103.
- KYRIAZIS, N., KOUKOUVINIS, P. & GAVAISES, M. 2019 Numerical investigations on bubble-induced jetting and shock wave focusing: application on a needle-free injection. *Proc. R. Soc. Lond. A* **475** (2222), 20180548.

- LAUTERBORN, W. & BOLLE, H. 1975 Experimental investigations of cavitation-bubble collapse in the neighbourhood of a solid boundary. *J. Fluid Mech.* **72** (2), 391–399.
- LI, T., ZHANG, A., WANG, S.-P., LI, S. & LIU, W.-T. 2019 Bubble interactions and bursting behaviors near a free surface. *Phys. Fluids* **31** (4), 042104.
- LINDAU, O. & LAUTERBORN, W. 2003 Cinematographic observation of the collapse and rebound of a laser-produced cavitation bubble near a wall. *J. Fluid Mech.* **479**, 327–348.
- MAHRAVAN, E. & KIM, D. 2021 Bubble collapse and jet formation inside a liquid film. *Phys. Fluids* **33** (11), 112102.
- MILLER, S.T., JASAK, H., BOGER, D.A., PATERSON, E.G. & NEDUNGADI, A. 2013 A pressure-based, compressible, two-phase flow finite volume method for underwater explosions. *Comput. Fluids* **87**, 132–143.
- MOON, J., MAHRAVAN, E. & KIM, D. 2024 Mutual interaction of a collapsing bubble and a nearby viscoelastic solid. *Phys. Rev. Fluids* **9** (4), 043603.
- PHILIPP, A. & LAUTERBORN, W. 1998 Cavitation erosion by single laser-produced bubbles. *J. Fluid Mech.* **361**, 75–116.
- REN, Z., HAN, H., ZENG, H., SUN, C., TAGAWA, Y., ZUO, Z. & LIU, S. 2023 Interactions of a collapsing laser-induced cavitation bubble with a hemispherical droplet attached to a rigid boundary. *J. Fluid Mech.* **976**, A11.
- ROBINSON, P.B., BLAKE, J.R., KODAMA, T., SHIMA, A. & TOMITA, Y. 2001 Interaction of cavitation bubbles with a free surface. *J. Appl. Phys.* **89** (12), 8225–8237.
- ROBLES, V., GUTIERREZ-HERRERA, E., DEVIA-CRUZ, L.F., BANKS, D., CAMACHO-LOPEZ, S. & AGUILAR, G. 2020 Soft material perforation via double-bubble laser-induced cavitation microjets. *Phys. Fluids* **32** (4), 042005.
- SIEBER, A.B., PRESO, D.B. & FARHAT, M. 2022 Dynamics of cavitation bubbles near granular boundaries. *J. Fluid Mech.* **947**, A39.
- SUN, Y., DU, Y., YAO, Z., ZHONG, Q., GENG, S. & WANG, F. 2022*a* The effect of surface geometry of solid wall on the collapse of a cavitation bubble. *J. Fluids Engng* **144** (7), 071402.
- SUN, Y., YAO, Z., WEN, H., ZHONG, Q. & WANG, F. 2022*b* Cavitation bubble collapse in a vicinity of a rigid wall with a gas entrapping hole. *Phys. Fluids* **34** (7), 073314.
- SUN, Y., ZHONG, Q., YAO, Z., ZI, D., XIAO, R. & WANG, F. 2023 Deflection of cavitation bubble near the rigid wall with a gas-containing hole. *J. Hydrodyn.* **35** (2), 330–337.
- SUPPONEN, O., OBRESCHKOW, D., TINGUELY, M., KOBEL, P., DORSAZ, N. & FARHAT, M. 2016 Scaling laws for jets of single cavitation bubbles. *J. Fluid Mech.* **38**, 263–293.
- THEODORAKOS, I., KALAITZIS, A., MAKRYGIANNI, M., HATZIAPOSTOULOU, A., KABLA, A., MELAMED, S., DE LA VEGA, F. & ZERGIOTI, I. 2019 Laser-induced forward transfer of high viscous, non-Newtonian silver nanoparticle inks: jet dynamics and temporal evolution of the printed droplet study. *Adv. Engng Mater.* **21** (10), 1900605.
- TOMITA, Y., ROBINSON, P.B., TONG, R.P. & BLAKE, J.R. 2002 Growth and collapse of cavitation bubbles near a curved rigid boundary. *J. Fluid Mech.* **466**, 259–283.
- TURKOZ, E., PERAZZO, A., KIM, H., STONE, H.A. & ARNOLD, C.B. 2018 Impulsively induced jets from viscoelastic films for high-resolution printing. *Phys. Rev. Lett.* **120** (7), 074501.
- VERHAAGEN, B. & RIVAS, D.F. 2016 Measuring cavitation and its cleaning effect. *Ultrason. Sonochem.* **29**, 619–628.
- VOGEL, A. & LAUTERBORN, W. 1988 Acoustic transient generation by laser-produced cavitation bubbles near solid boundaries. *J. Acoust. Soc. Am.* **84** (2), 719–731.
- VOGEL, A., LAUTERBORN, W. & TIMM, R. 1989 Optical and acoustic investigations of the dynamics of laser-produced cavitation bubbles near a solid boundary. *J. Fluid Mech.* **206**, 299–338.
- WANG, G., ZHANG, S., YU, M., LI, H. & KONG, Y. 2014 Investigation of the shock wave propagation characteristics and cavitation effects of underwater explosion near boundaries. *Appl. Ocean Res.* **46**, 40–53.
- WANG, Q. 2016 Local energy of a bubble system and its loss due to acoustic radiation. *J. Fluid Mech.* **797**, 201–230.
- WANG, Q., MAHMUD, M., CUI, J., SMITH, W.R. & WALMSLEY, A.D. 2020 Numerical investigation of bubble dynamics at a corner. *Phys. Fluids* **32** (5), 053306.
- WELLER, H.G. 2008 A new approach to VOF-based interface capturing methods for incompressible and compressible flow. *Tech. Rep.* TR/HGW/04. OpenCFD.
- WELLER, H.G., TABOR, G., JASAK, H. & FUREBY, C. 1998 A tensorial approach to computational continuum mechanics using object-oriented techniques. *Comput. Phys.* **12** (6), 620–631.

- YIN, J., ZHANG, Y., QI, X., TIAN, L., GONG, D. & MA, M. 2023 Numerical investigation of the cavitation bubble near the solid wall with a gas-entrapping hole based on a fully compressible three-phase model. *Ultrason. Sonochem.* **98**, 106531.
- ZENG, Q., GONZALEZ-AVILA, S.R., DIJKINK, R., KOUKOUVINIS, P., GAVAISES, M. & OHL, C.-D. 2018 Wall shear stress from jetting cavitation bubbles. *J. Fluid Mech.* **846**, 341–355.
- ZENG, Q., ZHANG, A.-M., TAN, B.H., AN, H. & OHL, C.-D. 2024 Jetting enhancement from wall-proximal cavitation bubbles by a distant wall. *J. Fluid Mech.* **987**, R2.
- ZHANG, J., DU, Y., LIU, J., SUN, Y., YAO, Z. & ZHONG, Q. 2022 Experimental and numerical investigations of the collapse of a laser-induced cavitation bubble near a solid wall. *J. Fluid Mech.* **34** (2), 189–199.